

EPITAXIAL GROWTH AND PROPERTIES OF KTaO_3 AND RELATED ALLOYS

By

HYUNG-JIN BAE

A DISSERTATION PRESENTED TO THE GRADUATE SCHOOL
OF THE UNIVERSITY OF FLORIDA IN PARTIAL FULFILLMENT
OF THE REQUIREMENTS FOR THE DEGREE OF
DOCTOR OF PHILOSOPHY

UNIVERSITY OF FLORIDA

2005

To my family for their love and passion.

ACKNOWLEDGMENTS

I thank my parents for encouraging and supporting me to keep pursuing my goals. Without them, I would not be in this position with my PhD degree. Also, I thank my sister, who helped me by living with me for two years while I was studying for qualifying exam. She made me concentrate on my study. Also, I thank my only brother-in-law, Dan for taking care of my sister and their son, my first nephew, Danny.

Also, I thank my host father and mother, Jan and Mike Martin, who was vice president in the College of Agricultural and Life Sciences, and is currently working as President at New Mexico State University. They helped me to settle down in Gainesville without feeling homesick my first year at UF, gave me great advice for my academic career. In addition, my host mom helped my sister plan and organize her wedding, and cared for her as a loving mother. I currently keep in touch with them, and I consider them my second family.

I have been honored to work with a marvelous advisor and group members here in the Materials Science and Engineering Department at the University of Florida.

I thank Dr. Norton, who has guided me to reach this position with his advice and support. And I would like to give my appreciation to my committee members : Dr. Cammy R. Abernathy, Dr. Stephen J. Pearton, , Dr. Susan Sinnott, and Dr. Toshikazu Nishida.

Finally, I would like to thank all of my former and present group members: Dr. Jennifer Sigman, Dr. Young-woo Heo, Dr. She-jin Park, Dr Yong-wook Kwon, George,

Matt, Hyun-sik, Charlee, Seemant, Ryan, Patrick, Li Chia, Yuanjie, and Daniel, who encouraged me.

TABLE OF CONTENTS

	<u>page</u>
ACKNOWLEDGMENTS	iii
LIST OF TABLES.....	viii
LIST OF FIGURES	ix
ABSTRACT	xiv
CHAPTER	
1 INTRODUCTION	1
2 LITERATURE REVIEW	5
2.1 Perovskite Materials	5
2.1.1 Origin and Structure of Perovskites	5
2.1.2 Various Properties of Perovskites	5
2.1.3 Applications	8
2.2 Properties of KTaO_3 , KNbO_3 , and $\text{K}(\text{Ta},\text{Nb})\text{O}_3$	8
2.3 Dielectric Properties	10
2.3.1 Capacitance and Polarization	10
2.3.2 Dielectric Loss	12
2.3.3 Dielectric Breakdown.....	13
2.3.3.1 Intrinsic Breakdown.....	13
2.3.3.2 Thermal Breakdown.....	14
2.4 Interdigital Electrode for Capacitance Measurements	14
2.5 Overview of Tunable Microwave.....	16
2.6 Pulsed Laser Deposition (PLD).....	17
2.6.1 Overview	17
2.6.2 PLD system configuration.....	18
2.6.2.1 Laser (Light Amplification by Stimulated Emission of Radiation).	18
2.6.2.2 Optics	21
2.6.2.3 Deposition System	22
2.6.3 Laser and Target Interaction (Phenomena inside deposition chamber)	22
2.6.4 Origin of Splashing	24
2.6.4 Background Gas Effect	26
2.7 Defect Chemistry	26
2.8 Characterization.....	29

2.8.1 X-Ray Diffraction (XRD).....	29
2.8.2 Four Circle XRD.....	30
2.8.3 Atomic Force Microscopy (AFM).....	30
2.8.4 Transmission Electron Microscopy (TEM)	31
2.8.5 Hall measurement.....	32
2.8.6 Capacitance and Voltage Measurements	33
3 SURFACE TREATMENT FOR FORMING UNIT-CELL STEPS ON THE (001)	
KTaO₃ SUBSTRATE SURFACE.....	48
3.1 Introduction	48
3.2 Experimental Methods	49
3.3 Results and Discussion.....	50
3.4 Conclusion.....	53
4 GROWTH OF SEMICONDUCTING KTaO₃ THIN FILMS	64
4.1 Introduction	64
4.2 Experimental Methods	65
4.3 Results and Discussion	66
4.4 Conclusion.....	68
5 DIELECTRIC PROPERTIES OF Ti-DOPED K(Ta,Nb)O₃ THIN FILMS GROWN	
 BY PULSED LASER DEPOSITION	73
5.1 Introduction	73
5.2 Experimental Methods	75
5.3 Results and Discussion.....	76
5.4 Conclusion.....	81
6 LOW DIELECTRIC LOSSES IN ANNEALED Ti-DOPED K(Ta,Nb)O₃ THIN	
 FILMS GROWN BY PULSED LASER DEPOSITION	95
6.1 Introduction	95
6.2 Experimental Methods	95
6.3 Results and Discussion.....	96
6.4 Conclusion.....	99
7 THICKNESS DEPENDENT TUNABILITY FOR Ti-DOPED K(Ta,Nb)O₃ FILM	
 BY PLD.....	110
7.1 Introduction	110
7.2 Experimental Methods	111
7.3 Results and Discussion.....	112
7.4 Summary	116
8 SUMMARY.....	129

LIST OF REFERENCES.....	131
BIOGRAPHICAL SKETCH.....	143

LIST OF TABLES

<u>Table</u>	<u>page</u>
1-1. Substrates for ferroelectric oxide	4
2-1. Applications of Perovskites in Materials	8
2-2. Excimer laser operating wavelength	20
2-3. Transmittance range for various lens and window materials	22

LIST OF FIGURES

<u>Figure</u>	<u>page</u>
2-1. Perovskite structure	34
2-2. Ferroelectric hysteresis loop.....	34
2-3. Dielectric constants as a function of temperature for KNbO_3	35
2-4. Application fields and fundamental technical terms in future oxide electronics	35
2-5. Schematic diagrams of (a) Parallel plate capacitor of area A and separation d in vacuum attached to a voltage source and (b) parallel plate capacitor with dielectric material between two plates	36
2-6. Definition of electric dipole moment	37
2-7. Schematic representation of different mechanisms of polarization	38
2-8. Frequency dependence of several contributions to the polarizability	39
2-9. Applied voltage, charging, loss, and total currents for a capacitor	39
2-10. Schematic diagram of several capacitor measurement techniques	40
2-11. Schematic diagram of (a) Interdigital capacitor (IDC) structure and (b) top electrodes	41
2-12. Schematic diagrams of photon interaction to produce laser; (a) non-lasing State, (b) excitation of atoms using light source, (c) photon emission, (d) stimulated emission of further photons, and (e) column of laser light leaving optical oscillator.....	42
2-13. Schematic diagram of pulsed laser system (PLD)	43
2-14. Various type of defects typically found in ceramics. Misplaced atoms can only occur in covalent ceramics due to charge considerations	44
2-15. Bragg's law	45
2-16. Geometry of four circle x-ray.....	45

2-17. Schematic diagram of atomic force microscopy	46
2-18. Schematic diagram of the geometry of Van der Pauw measurements; (a) resistivity, and (b) Hall constant, R_H	47
3-1. AFM image of a chemically-mechanically polished KTaO_3 surface.....	54
3-2. AFM images of a KTaO_3 surface that was: (a) annealed at 900°C for 4h, and (b) annealed at 1000°C for 4h.....	55
3-3. AFM images of a KTaO_3 surface that was: (a) etched 18min only, and (b) etched 15min, then annealed 700°C for 3h.....	56
3-4. AFM images of surface-treated KTaO_3 as a function of etching time with BOE and then annealed at 700°C for 4 h: (a) 12 min, (b) 15 min, (c) 30 min ($5\mu\text{m} \times 5\mu\text{m}$), and (d) surface section in (b).....	57
3-5. RMS surface roughness values of surface-treated KTaO_3 as a function of etching time with BOE and then annealed at 700°C for 4 h.	58
3-6. AFM images of surface-treated KTaO_3 as a function of etching time with BOE and then annealed at 900°C for 4 h : (a) without etching, (b) 2 min, (c) 5 min, and (d) 30 min ($1\mu\text{m} \times 1\mu\text{m}$)	59
3-7. Enlarged AFM image of KTaO_3 etched with BOE for 2 min followed by annealing at 900°C ($1\mu\text{m} \times 1\mu\text{m}$).....	60
3-8. RMS surface roughness values of surface treated KTaO_3 as a function of etching time with BOE and then annealed at 900°C for 4 h.	61
3-9. AFM images of a KTaO_3 single crystal surface annealed at 1000°C for 1 h (a) without etching and (b) after etched in BOE for 10min.	62
3-10. AFM images of a KTaO_3 single-crystal surface that was (a) etched in BOE for 18min, then annealed at 700°C for 3 h with KTaO_3 powder. The RMS roughness was 1.385nm (RMS of particle-free area : 0.450 nm). Also shown (b) are AFM images of a KTaO_3 surface that was etched in BOE for 8min and then annealed at 1000°C for 3 h with KTaO_3 powder. The RMS was 4.980nm, (in the particle-free area : 0.580 nm).....	63
4-1. Schematic diagram of the segmented $\text{KTaO}_3/\text{KNO}_3$ target	69
4-2. X-ray diffraction results of KTaO_3/Ca film grown on MgO (100) substrate as a function of deposition temperature.	69
4-3. X-ray diffraction results of KTaO_3/Ca film grown on MgO (100) substrate as a function of different oxygen pressure at deposition temperature of 700°C	70

4-4. X-ray diffraction results of Ca doped KTaO ₃ semiconducting film grown on MgO (100) substrate at deposition temperature of 700 °C in reduced pressure of 96% Ar/4% H ₂	70
4-5. X-ray diffraction Phi scan and rocking curve data.....	71
4-6. FE-SEM images of surface morphology of semiconducting KTO:Ca film on (100) MgO substrate, which was deposited at 700°C for 1hr with 30mTorr of 96%Ar/4% H ₂ mixture gas using pulsed laser deposition.	72
4-7. Resistivity of Ca doped KTaO ₃ thin film as a function of temperature.	72
5-1. XRD results of KTN:Ti films grown at different growth temperature with 100mTorr of oxygen atmosphere and 1Hz of frequencies.....	82
5-2. XRD results of KTN:Ti films grown at different oxygen pressure with deposition temperature 750°C.	83
5-3. Four circle XRD results of KTN:Ti films grown at 100mTorr oxygen pressure with deposition temperature 750°C. (a) phi scan for the (111) reflection of KTN:Ti and MgO, and (b) the rocking curve of (200) KTN:Ti film: FWHM is 0.564°.	84
5-4. TEM images of KTN:Ti films grown on MgO single crystals at 750°C of growth pressure, and 100mTorr of oxygen atmosphere.....	85
5-5. AFM images of KTN:Ti films grown at different oxygen pressure with deposition temperature 750°C : (a) vacuum, (b) 50mTorr (c) 100mTorr and (d) 150mTorr	86
5-6. Results of capacitance of KTN:Ti films on MgO single crystals as a function of oxygen growth pressure under 0, 10,20, 35, and 40V dc bias voltage measured at 30°C, and frequency of 1MHz	87
5-7. Oxygen pressure dependence of capacitance for KTN:Ti films on MgO single crystals under temperature in the range of 50 – 240°C at dc bias of 10V, and frequency of 1MHz.....	88
5-8. Oxygen pressure dependence of loss tangent for KTN:Ti film on MgO single crystal under dc bias in the range of 0 – 40kV/cm at temperature of 30°C, and frequency of 1MHz.....	89
5-9. DC bias voltage dependence of (a) capacitance and (b) tunability for KTN:Ti film on MgO at room temperature at 1MHz frequency. KTN:Ti film was grown at 150mTorr of oxygen with deposition temperature 750°C	90
5-10. Tunability $(= (C(E_0) - C(E_{max})) / C(E_0) \times 100)$ and loss tangent of KTN:Ti film grown on (001) MgO at different growth pressure with deposition temperature 750°C.....	91

5-11. Figure of merit (FOM=tunability/loss tangent) of KTN:Ti film grown on (001) MgO at different growth pressure with deposition temperature 750°C.....	92
5-12. Capacitance and tunability of KTN:Ti film as a function of measurement temperature. KTN:Ti film was grown on (001) MgO at deposition temperature 750°C, and 150mTorr of oxygen atmosphere	93
5-13. Comparison of loss tangent of undoped KTN and KTN:Ti film as a function of measurement temperature. Both films were grown on (001) MgO at 750°C of deposition temperature, and 100mTorr of oxygen atmosphere for 1hr. (■: loss tangent of KTN, ●: loss tangent of KTN:Ti films).....	94
6-1. XRD results of KTN:Ti films annealed at different temperatures. KTN:Ti films were grown at 750°C of deposition temperature, and 100mTorr of oxygen pressure	100
6-2. Lattice spacing of KTN:Ti films annealed at different temperatures.....	101
6-3. Four circle XRD results of KTN:Ti film annealed at 900°C for 2hrs. KTN:Ti film was grown at 100mTorr oxygen pressure with deposition temperature 750°C. (a) phi scan for the (110) reflection of KTN:Ti and MgO, and (b) the rocking curve of (200) KTN:Ti film: FWHM is 0.566°	102
6-4. AFM images of KTN:Ti films annealed at different temperature with oxygen ambient for 2hrs. Growth condition of KTN:Ti films were 750°C deposition temperature, 100mTorr of oxygen pressure and 1Hz of frequencies : (a) without annealing, (b) annealed at 800°C, (c) annealed at 900°C, and (d) annealed at 1000°C.....	103
6-5. Results of tunabilities of as-deposited and annealed KTN:Ti films as a function of measurement temperature. Tunability $((C(E_0)-C(E_{max}))/C(E_0) \times 100)$ was measured at 0 - 40kV/cm of electric field range, 1MHz frequency.....	104
6-6. Results of dielectric loss of as-deposited and annealed KTN:Ti films as a function of measurement temperature	105
6-7. Results of capacitance and FOM for KTN:Ti film on MgO annealed at 900°C for 2hrs at room temperature as a function of electric field	106
6-8. Temperature dependence of capacitance for KTN:Ti film on MgO at temperature of 20°C at 1MHz frequency under different electric field ranging 0 - 40kV/cm. KTN:Ti film was grown at 100mTorr of oxygen with deposition temperature 750°C and then annealed at 900°C for 2hrs	107
6-9. Temperature dependence of dielectric loss for KTN:Ti film on MgO at temperature of 20°C at 1MHz frequency under different electric field ranging 0 - 40kV/cm. KTN:Ti film was grown at 100mTorr of oxygen with deposition temperature 750°C and then annealed at 900°C for 2hrs	108

6-10. Comparison of FOM of as – deposited and 900°C annealed KTN:Ti films on MgO with different measurement temperature at 1MHz frequency	109
7-1. XRD results of KTN:Ti films on (100) MgO substrates grown at 750 °C, 100 mTorr of oxygen ambient with different film thicknesses.....	117
7-2. AFM images for surface morphologies of KTN:Ti films on (100) MgO substrates : (a) 90 nm, (b) 180 nm, and (c) 250 nm of KTN:Ti film thickness. AFM images taken in area of 3 x 3 µm using contact mode	118
7-3. Capacitance as a function of the thickness of KTN:Ti film under different measurement temperatures.....	119
7-4. Capacitance data of KTN:Ti films on MgO (100) as a function of applying electric field up to ± 40kV/cm with different film thicknesses.....	120
7-5. Tunabilities of KTN:Ti films as a function of electric field with different film thicknesses	121
7-8. FOM of KTN:Ti films as as a function of electric field with different film thicknesses	124
7-9. Capacitance results of KTN:Ti film grown at 750°C and 100mTorr oxygen ambient on (001) MgO substrate as a function of capacitance measurement temperature	125
7-10. Dielectric loss of KTN:Ti film as a function of capacitance measurement temperatures under different film thicknesses	126
7-11. Tunability of KTN:Ti film as a function of capacitance measurement temperatures under different film thicknesses	127
7-12. FOM of KTN:Ti film as a function of capacitance measurement temperatures under different film thicknesses.....	128

Abstract of Dissertation Presented to the Graduate School
of the University of Florida in Partial Fulfillment of the
Requirements for the Degree of Doctor of Philosophy

EPITAXIAL GROWTH AND PROPERTIES OF KTaO_3 AND RELATED ALLOYS

By

Hyung-Jin Bae

May 2005

Chair: David Norton

Major Department: Materials Science and Engineering

KTaO_3 , KNbO_3 and solid solution $\text{K}(\text{Ta,Nb})\text{O}_3$ are interesting ferroelectric materials due to their possible applications for FRAM, optical wave-guide, and tunable microwave devices. By controlling the concentration of Nb in $\text{KTa}_{1-x}\text{Nb}_x\text{O}_3$, it is possible to modify the Curie temperature, T_c , of $\text{KTa}_{1-x}\text{Nb}_x\text{O}_3$.

An atomically flat surface of a substrate is very important to grow thin films with minimal defect on the top of the substrates. So, we studied a method for the preparation of unit-cell-high steps on the (100) surface of KTaO_3 . The effects of various surface treatments on the (100) KTaO_3 surface, specifically the chemical etching and annealing characteristics, are discussed. Surface step formation was observed for KTaO_3 single crystals that were subjected to buffered HF etching followed by annealing in air. The resulting surface morphology of (001) KTaO_3 was examined using atomic force microscopy. The role of etching time and annealing temperatures in determining the resulting step structure, roughness, and particulate formation on the KTaO_3 surface was discussed.

We also studied the synthesis and semiconducting properties of cation and defect-doped KTaO_3 films. The Ca doped and defect doped KTaO_3 films were grown on (100) MgO single crystal substrates using pulsed-laser deposition. Semiconducting behavior was achieved by inducing oxygen vacancies in the KTaO_3 lattice via growth in a hydrogen atmosphere. The resistivity of semiconducting $\text{KTaO}_3\text{:Ca}$ films was as low as $10\ \Omega\text{cm}$, and n-type semiconducting behavior was indicated. Hall mobility and carrier concentration were $0.27\ \text{cm}^2/\text{Vs}$ and $3.2 \times 10^{18}\ \text{cm}^{-3}$, respectively. Crystallinity and microstructure of the $\text{KTaO}_3\text{:Ca}$ films were examined using X-ray diffraction and field-emission scanning electron microscopy.

We have investigated the growth and dielectric properties of K(Ta,Nb)O_3 films doped with Ti. Titanium (+4) substitution on the group V (Nb/Ta) site should introduce an acceptor state, thus reducing dielectric losses due to defect-induced donor states. Using 3% Ti-doped targets, $\text{K(Ta,Nb)O}_3\text{:Ti}$ films were grown on MgO (001) crystals using pulsed-laser deposition. A reduction in the loss tangent was observed for Ti-doped K(Ta,Nb)O_3 relative to undoped films, although a reduction in tunability was also seen. In addition, the films were annealed in oxygen at temperatures as high as 1000°C . A loss tangent of 0.002 at room temperature was observed for annealed Ti-doped K(Ta,Nb)O_3 . A reduction in tunability was also observed. For these annealed films, the dielectric loss showed little temperature dependence, indicating significant reduction in donor density due to defects. The crystallinity, morphology, dielectric constant, and tunability of $\text{K(Ta,Nb)O}_3\text{:Ti}$ films were reported.

CHAPTER 1 INTRODUCTION

Perovskite materials have been intensively studied due to their piezoelectric, pyroelectric, ferroelectric, and electro-optic properties. These properties make perovskite materials attractive for various applications such as ferroelectric random access memory (FRAM), sensors, actuators, waveguide, and microwave devices.

Bulk materials for some applications have been investigated. For semiconducting technology, thin films are studied for device applications.

Ferroelectric materials can be grown in the form of an oxide thin film on a variety of substrates using liquid phase epitaxy^{1,2}, sol-gel³⁻⁵, ion beam sputter-deposition (IBSD)^{6,7}, molecular beam epitaxy(MBE)⁸⁻¹¹, pulsed laser deposition (PLD)¹², metalorganic chemical vapor deposition (MOCVD)¹³⁻¹⁹.

Growth of ferroelectric thin films on oxide single crystal has received significant attention. Table 1-1 shows available substrates for the growth of high temperature superconductor (HTS) and ferroelectric thin films. For epitaxial growth, lattice parameters and thermal expansion coefficient of substrates and films are important because they affect the microstructure of the film in terms of lattice strain, misfit dislocations, and defects. KNbO_3 , SrTiO_3 , and $(\text{Ba,Sr})\text{TiO}_3$ films have been grown epitaxially on MgO and LaAlO_3 ²⁰⁻²².

In order to grow better quality thin films and heterostructures of complex oxides with atomically flat surfaces and sharp interfaces, well-controlled layer-by-layer or step flow growth is required. Crystallinity of the films for above mentioned growth modes

depends on the quality of the substrate surfaces. There have been many investigations to realize atomically flat surfaces on SrTiO_3 , NdGaO_3 , and LaAlO_3 ²³⁻²⁵. Atomically flat surfaces have been achieved with the above mentioned perovskite materials with the ABO_3 structure because of two possible terminating atomic layers – AO (A-site layer) and BO_2 (B-site layer) on the $\{001\}$ surfaces. Therefore, KTaO_3 single crystals with ABO_3 structure can be studied to obtain atomically flat surfaces with unit cell high step structure by terminating with K-O or Ta-O layers. By forming the step structures on the substrate surface, quantum wire or superlattices can be grown. For this, etching and annealing studies using (001) KTaO_3 single crystals will be conducted.

Also, some oxide materials such as SrTiO_{3-x} , and Nb doped SrTiO_3 show semiconducting behavior due to oxygen vacancies. With these properties, oxide materials can potentially be fabricated for channel layer of FET or other devices.

$(\text{Ba,Sr})\text{TiO}_3$ has been studied for FRAM and tunable microwave devices due to its ferroelectric properties. For tunable microwave applications, ferroelectric materials should be in the paraelectric region just above the Curie temperature, T_c , because in this region materials do not have large dielectric losses due to spontaneous polarization, but still retain their high dielectric constants.

KTaO_3 and $\text{K}(\text{Ta,Nb})\text{O}_3$ are of interest for tunable microwave applications due to their high dielectric constant, low dielectric loss, and composition dependence of Curie temperature. With the previously mentioned properties, KTaO_3 , KNbO_3 , and $\text{K}(\text{Ta,Nb})\text{O}_3$ can replace BST for various applications. Therefore, in chapter 2, the structure and properties of KTaO_3 , KNbO_3 , and $\text{K}(\text{Ta,Nb})\text{O}_3$ will be briefly reviewed. Surface modification of a KTaO_3 single crystal for atomically flat surface is discussed in chapter

3. Chapter 4 describes semiconducting properties of KTaO_3 thin film by Ca and defect doping in reduced condition using 4% H_2/Ar gas. From chapter 5 to 7, dielectric properties of $\text{K}(\text{Ta,Nb})\text{O}_3$ films by acceptor (Ti^{+4}) doping in Ta or Nb sites will be discussed. In chapter 5, dielectric properties of Ti doped $\text{K}(\text{Ta,Nb})\text{O}_3$ (KTN:Ti) film on (001) MgO substrates with various growth conditions such as growth temperature and oxygen pressure are covered. The annealing effect on dielectric properties of KTN:Ti film is discussed in chapter 6. Finally, Thickness effect of KTN:Ti film for dielectric properties is discussed in chapter 7. In chapter 8, the conclusion will be presented about the results of the experiments.

Table 1-1. Substrates for ferroelectric oxide

Materials	Crystal symmetry	Lattice Constant (Å)	α^a (1/K)	ϵ	Loss tangent ^c	Price (\$)
LaAlO ₃	Pseudo-cubic	a=3.972	$\sim 10 \times 10^{-6}$	25	6×10^{-5}	40
MgO	cubic	a=4.203	8×10^{-6}	9.7	3.3×10^{-7}	20
Al ₂ O ₃	Hexagonal	a=4.763 c=13.0	8×10^{-6} 13×10^{-6}	9.9	6×10^{-5}	20
YBa ₂ Cu ₃ O _{7-x}	Orthorhombic	a=3.82 b=3.89 c=11.68	14×10^{-6} 12×10^{-6} 25×10^{-6}			
SrTiO ₃	Cubic	a=3.905	8.63×10^{-6}	$>300^b$	$<10^{-3}$	50
NdGaO ₃	Orthorhombic	a=5.515 b=5.499 c=7.710		22^b	3×10^{-4}	65
LaGaO ₃	Orthorhombic	a=5.519 b=5.494 c=7.77	10.6×10^{-6}	25	1×10^{-4}	
CaNdAlO ₄	Tetragonal	a=3.688 c=12.15		20	1×10^{-4}	80
YSZ	Cubic	a=5.16	10×10^{-6}	27^a		20
Mg ₂ TiO ₄	Cubic	a=8.44	12×10^{-6}	12	1.5×10^{-4}	
MgAl ₂ O ₄	Cubic	a=8.086	7.6×10^{-6}			30
PrGaO ₃	Orthorhombic	a=5.462 b=5.4943 c=7.740	8.36×10^{-6} 7.31×10^{-6} 6.99×10^{-6}	24^d	3.6×10^{-4} \sim 5.4×10^{-3}	
Y ₂ O ₃	Cubic	a=10.60		9 - 17		
Si	Cubic	a=5.43	2.6×10^{-6}	12^a		8
GaAs	Cubic	a=5.65	2.86×10^{-6}	13^a		120*
KTaO ₃	Cubic	a=3.988	$\times 10^{-6}$			225

^a At room temperature, ^b At 1GHz and 77K, ^d At 1MHz and 77K, α : thermal expansion coefficient, * 2 inch wafer

CHAPTER 2 LITERATURE REVIEW

2.1 Perovskite Materials

2.1.1 Origin and Structure of Perovskites

There are many families of crystalline classes based on their crystal structures such as rock salts, spinel, rutile, wurtzite, and perovskite. Among these crystalline classes, the name “perovskites” is derived from a specific mineral known as a perovskite.

The principal perovskite structure (shown in Figure 2-1) found in ferroelectric materials is a simple cubic structure containing three different ions of the form ABO_3 . The A and B atoms usually represent +2 and +4 ions, respectively, while the O atom is the oxygen ion. This ABO_3 structure in a general sense can be considered as face centered cubic (FCC) lattice with A atoms at the corners and O atoms on the faces. The B atom is located at the center of the lattice, which is known as an octahedral site surrounded by 6 oxygen ions. This A atom is the largest of the atoms and consequently increases the overall size of the AO_3 (FCC) structure. As a result, there are minimum energy positions off-centered from the original octahedron that can be occupied by the B atom. Shifting of this atom due to applied electric fields causes the structure to be altered, creating electric dipoles.

2.1.2 Various Properties of Perovskites

Perovskite materials have various physical and electrical properties. This extends to a wide range of applications in discrete devices, utilizing the full range of properties, including dielectric, ferroelectric, piezoelectric, electrostrictive, pyroelectric, electro-

optic, and magnetic properties in addition to superconductivity. Also, some perovskites materials exhibit more than one property. For example, $\text{Ba}_x\text{Sr}_{1-x}\text{TiO}_3$ shows behaviors of piezoelectric, ferroelectric, and paraelectric properties²⁶. Several properties of perovskites and representative materials for the properties will be addressed here.

Piezoelectric materials such as quartz, LiNbO_3 ²⁷, LiTaO_3 ²⁷⁻²⁹, BaTiO_3 ^{30,31}, and $\text{Pb}(\text{ZrTi})\text{O}_3$ ³²⁻³⁵ produce electric charges on their surfaces as a consequence of applying a mechanical stress. The induced charges are proportional to the mechanical stress. This is called the “direct piezoelectric effect.” Materials showing this phenomenon also conversely have a geometric strain proportional to an applied electric field. This is the “converse piezoelectric effect.” The root word “piezo” means “pressure”; hence the original meaning of the word piezoelectricity implies “pressure electricity.” Piezoelectricity is extensively utilized in the fabrication of various devices such as transducers, actuators, surface acoustic wave devices, and frequency controllers.

Pyroelectric materials such as LiTaO_3 ³⁶, $\text{Sr}_{1/2}\text{Ba}_{1/2}\text{Nb}_2\text{O}_6$ ^{37,38}, and PLZT ³⁹ are referred as “electric stones.” Pyroelectricity could be divided into true pyroelectricity and false pyroelectricity. True pyroelectricity is the development of electric charges of opposite sign at opposite ends of an unstressed crystal, which is heated (or cooled) uniformly. False pyroelectricity is the similar development of charges when there is a temperature gradient or when the heated crystal becomes subject to stress. These two pyroelectricities are difficult to distinguish. However, true pyroelectricity implies a resultant vector in the crystal and can therefore only occur in the polar classes. False pyroelectricity and piezoelectricity must be described by tensors, so the above argument does not apply. They can occur in any crystal class which lacks a center of symmetry

except the cubic class. This pyroelectricity is basically due to the temperature dependence of the spontaneous polarization of a polar material. These materials can be used as temperature sensors and infrared light detectors.

Some perovskite materials, such as KTaO_3 , can be used in electro-optic devices because the refractive index is changed by applying an external electric field. As a result, these materials have been applied in light valves, beam reflectors, and optical displays for optical communication with solid state laser chips and optical fibers due to high response speed and resistance over high intensity illumination.

Ferroelectric materials such as BaTiO_3 , SrTiO_3 , and KNbO_3 show spontaneous polarizations that are caused by asymmetric displacement of center ion in unit cell. BaTiO_3 is the representative material for this ferroelectric property⁴⁰. Most ferroelectric materials have ferro- to paraelectric transition temperature. This temperature is called Curie temperature, T_c . In the paraelectric state, i.e., above T_c , the net dipole moment is zero in the material if an electric field is not applied. However, if an electric field is applied to the material, dipole moments are aligned parallel to the electric field and this paraelectric material has a high dielectric constant.

Ferroelectric properties include:

- ▶ A dielectric hysteresis loop, indicating reversible spontaneous polarization shown in Figure 2-2,
- ▶ Disappearance of hysteresis loop above Curie temperature,
- ▶ A domain structure, which may be visible in polarized light,
- ▶ A high dielectric constant, rising to a peak at the Curie temperature (Figure 2-3⁴¹),
- ▶ The falling-off of the dielectric constant above the Curie temperature, which

follows a Curie-Weiss law,

- ▶ A pseudosymmetric structure,
- ▶ A ferroelectric symmetry that places them in a polar class,
- ▶ A transition at the Curie temperature to a form of higher symmetry,
- ▶ The Curie temperature, which is raised (or lowered) by the application of a biasing field,
- ▶ A sudden appearance of surface charges at the transition.

2.1.3 Applications

Perovskites materials can be used in various application fields with above mentioned properties. Table 2-1 shows specific applications and commonly used materials for the applications. For those applications, perovskite materials can be utilized in a form of bulk or thin film. However, with the advancement of Si (semiconducting) technology, many thin films for oxide electronic are investigated currently. Figure 2-4 shows various oxide application fields and fundamental technical terms in future oxide electronics.

2.2 Properties of KTaO_3 , KNbO_3 , and $\text{K}(\text{Ta,Nb})\text{O}_3$

Most perovskites have high electrical resistivities, which make them useful as dielectrics. However, some perovskites are considered to be good conductors, such as SrRuO_3 . Perovskite KTaO_3 ⁴² is an incipient ferroelectric material of cubic structure and it shows paraelectricity for all ranges of temperature. The lattice constant of KTaO_3 is 3.9885 Å at 300K and dielectric constants are 243 at 200 kHz, 300K and 4500 at 200 kHz, 4.2K. In contrast, KNbO_3 ^{43,44} exhibits a first-order ferroelectric phase transition accompanied by a change from the cubic to the tetragonal structure at 701K ($a_p=4.02\text{Å}$ along [100]p and [010]p directions, and $c_p=3.97\text{Å}$ along [001]p). Upon further cooling,

Table 2-1. Applications of perovskites in materials

<i>Applications</i>	<i>Perovskite Materials</i>
Multilayer Capacitor	BaTiO ₃
Piezoelectric Transducer	Pb(Zr,Yi)O ₃
P. T. C. Thermistor	BaTiO ₃
Electro-optical Modulator	(Pb, La)(Zr, Ti)O ₃
Switch	LiNbO ₃
Dielectric Resonator	BaZrO ₃
Thick Film Resistor	BaRuO ₃
Electrostrictive Actuator	Pb(Mg,Nb)O ₃
Superconductor	Ba(Pb,Bi)O ₃ layered cuprates
Magnetic Bubble Memory	GdFeO ₃
Laser Host	YAlO ₃
Ferromagnet	(Ca,La)MnO ₃
Refractory Electrode	LaCoO ₃
Second Harmonic Generator	KNbO ₃

the structure changes to orthorhombic at 498K, with lattice parameters $a = 5.696\text{\AA}$, $b = 5.7213\text{\AA}$, and $c = 3.9739\text{\AA}$. For the ferroelectric state, the polarization direction is along the [010]. It is important to note that the cubic KTaO_3 is well lattice matched to the cubic and tetragonal KNbO_3 , as the pseudo-cubic lattice parameter of KNbO_3 ($a_p = 4.014\text{\AA}$, $T = 25^\circ\text{C}$) differs from that of KTaO_3 by only 0.6%.

The $\text{K}(\text{Ta},\text{Nb})\text{O}_3$ system, like the $(\text{Sr},\text{Ba})\text{TiO}_3$ system, forms a solid solution. These mixed ferroelectric systems can show very different properties from those of simple ferroelectrics. For instance, the $\text{KTa}_{1-x}\text{Nb}_x\text{O}_3$ system^{45,46} has a diffuse phase transition with a continuously varying Curie temperature, T_c , according to the formula $T_c = 676x + 32$ (for $x > 4.7\%$). For $x > 0.35$, $\text{KTa}_{1-x}\text{Nb}_x\text{O}_3$ (KTN) shows a first-order ferroelectric phase transition similar to KNbO_3 . This ferroelectric phase transition is accompanied by the appearance of a remnant polarization due to off-center asymmetry of Nb and Ta ions. For $x < 0.35$, dielectric and polarization measurements suggest a diffuse character for the ferroelectric transition. There are two steps by which the transition in this range takes place. First, a progressive appearance of polar cells around single or groups of Nb ions occurs. Second, the collective ordering of the individual electric dipoles occurs due to mutual strain between cells.

2.3 Dielectric Properties

2.3.1 Capacitance and Polarization

Two metal plates of area A are separated with distance d in vacuum. When applying voltage to these two plates with closed circuit structure (Figure 2-5 (a)), abrupt current occurs and then rapidly decays to zero.

$$Q = \int I \, dt$$

The area under the I versus t curve is the total charge that has passed through the circuit and is now stored on the capacitor plates.

If applying different voltage to the circuit and then plotting Q versus V, a straight line is obtained. The following relationship is obtained:

$$Q=CV$$

The slope of the above relationship, C, is called the capacitance C_{vac} of the parallel plates in vacuum.

$$C_{vac} = \frac{\epsilon_0 A}{d}$$

where ϵ_0 is the permittivity of free space, which is a constant equal to 8.85×10^{-12} (F/m)

The relative dielectric constant of a material k' is defined as $k' = \epsilon/\epsilon_0$, ($k' \geq 1$).

$$C = \frac{k' \epsilon_0 A}{d} = k' C_{vac}$$

Thus k' is a unitless parameter that compares the charge-storing capacity of a material to that of vacuum.

Surface charge with presence of dielectric (Figure 2-5(b)) is described as follows

$$\left[\frac{Q}{A}\right]_{die} = \frac{\epsilon_0 k' V}{d} = \sigma_{vac} + \sigma_{pol}$$

where σ_{pol} is the excess charge per unit surface area present on the dielectric surface, and considered to be the same as polarization P of the dielectric.

Dielectric displacement D is defined to the surface charge on the metal plates,

$$D = \left[\frac{Q}{A}\right]$$

$$\therefore D = \epsilon_0 E + P$$

Dipole moment, μ

$$\mu = q\delta$$

where δ is the separation distance between positive and negative charge shown in Figure 2-6 .

$$k' - 1 = \frac{P}{\epsilon_0 E} = \frac{Nq\delta}{\epsilon_0 E}$$

This result gives us fundamental information to understand the dielectric response of a solid. The greater δ , which indicates the separation of the charges of a dipole for a given applied field, is, the greater k' , the relative dielectric constant, is. In other words, the more polarizable a medium is, the greater its dielectric constant.

There are several possible mechanisms for polarization in dielectric materials. Figure 2-7 shows possible mechanisms of polarization; electronic polarization, ionic polarization, orientation polarization, and space charge polarization⁴⁷. Also, these polarizations are dependent on frequencies. Therefore, by increasing frequency only fast reacting polarization at that frequency level can participate to response. Figure 2-8 shows the total polarizability as a function of frequencies.

2.3.2 Dielectric Loss

In ideal dielectric, the current caused by applied field has 90° out of phase based on applied field, which means the oscillating charges are in phase with the applied voltage.

$$I_{chg} = -\omega k' C_{vac} V_0 \sin \omega t$$

However, in reality the currents of charges are never in phase because of the energy dissipation and ohmic contact. Therefore, total current in real dielectric will lead

the applied voltage by angle $90^\circ - \phi$. ϕ is called the loss angle or loss tangent or dissipation factor⁴⁸. This is shown in Figure 2-9.

Relative dielectric constant can be expressed using a complex equation, which is the sum of real part and imaginary part.

$$k^* = k' - ik''$$

Also, loss tangent is the ratio of imaginary part to real part of dielectric constant.

$$\tan \phi \approx \frac{k''}{k'}$$

The charges in dielectric material will respond with ac electric field. There are two kinds of response of charges in material to contribute to k' and k'' . When some of the bound charges oscillate in phase with the applied field, this movement will result in charge storage and contribute to k' . When bound charges and those contributing dc conductivity oscillate 90° out of phase with applied electric field in dielectric material, these movements of charges result in dissipation of energy as a form of heat in dielectric material. The energy dissipation is proportional to loss angle ϕ . Dielectric loss is a measurement of the energy dissipated in dielectric material in unit time when electric field is applied.

$$P_v = \frac{1}{2} \{ \sigma_{dc} + \omega \epsilon_0 k''(\omega) \} E_0^2$$

2.3.3 Dielectric Breakdown

2.3.3.1 Intrinsic Breakdown

By applying an electric field, electrons in the conduction band are accelerated and start to ionize lattice ions by collision. The number of electrons is increased as more ions are ionized. Finally, an avalanche effect is created.

2.3.3.2 Thermal Breakdown

The rate of heat generation by dielectric loss in dielectric material is larger than the rate of heat removal from the dielectric material. Whenever this condition occurs the dielectric material will heat up and increase its conductivity.

2.4 Interdigital Electrode for Capacitance Measurements

Conventional capacitance measurements are conducted with parallel capacitance structure. Also, there are several measurement techniques such as coplanar waveguides (CPW), resonators, gaps in microstrip, and interdigital capacitors (IDC). Figure 2-10 shows the structures of several capacitor measurements including parallel capacitors, coplanar waveguides, resonators, and IDC (Figure 2-11). Dielectric materials for these measurements are usually polycrystalline, which has many defects such as oxygen vacancies, impurities, grain boundaries, and other defects. These defects affect the dielectric properties. One way to reduce these problems is to grow epitaxial thin films on single crystal. By growing epitaxial thin films on single crystals such as SrTiO_3 , MgO , MgAl_2O_4 , and LaAlO_3 , grain boundary, interface strain, and impurities problems can be solved or significantly reduced. Epitaxial thin films for microwave devices must be single-phase solution without secondary phases, good crystalline with a dense microstructure with minimal defects, and compositionally uniform. Also, the film-substrate interface must be abrupt, and thermally, chemically, and mechanically stable with respect to processing and device environmental conditions. Finally, the surface morphology must be compositionally uniform, morphologically smooth and defect or crack free.

To measure the dielectric properties of these structures (epitaxial thin films on single crystals), interdigitated electrodes are required on top of the epitaxial thin film.

Gevorgian⁴⁹ reported modeling of thin film HTS/ferroelectric interdigital capacitors in 1996. Many studies using interdigitated electrodes based on his modeling have been investigated⁵⁰⁻⁵².

Figure 2-11 shows the schematic diagram of the interdigital capacitor structure. To use the interdigital capacitor, several things need to be assumed. First, the dimension of the IDC is much less than the wavelength in the microwave devices, which is around 2cm, and there is no capacitance contribution from nonadjacent fingers. The capacitance of this two-layered substrate IDC is assumed to be a sum of partial capacitances due to air, a substrate with an equivalent dielectric constant (ϵ_1-1), and a superstrate with a dielectric constant ($\epsilon_2 - \epsilon_1$). Moreover, the capacitance of an IDC with finger number $n \geq 3$ is presented as a sum of the capacitances C_n of the periodic ($n - 3$) structures enclosed between the magnetic walls AA' and BB'⁴⁹.

Total capacitance C is a sum of all following partial capacitances.

$$C = C_3 + C_n + C_{end}$$

where C_3 is from a three finger capacitor, and C_{end} is a correction term for the fringing fields at the end of the strips.

$$C_n = (n-3)\epsilon_0\epsilon_n \frac{K(k_0)}{K(k'_0)} l$$

$$C_{end} = 4\pi(2+\pi)\epsilon_0\epsilon_{end} \frac{K(k'_{0end})}{K(k_{0end})}$$

$$C_3 = 4\epsilon_0\epsilon_3 \frac{K(k'_{03})}{K(k_{03})} l$$

where $k_x = s/(s+g)$ (where s is electrode width, and g is gap between electrodes) and $k'_x = \sqrt{1-k_x^2}$ (where x is 0, 0end, and 03) are the moduli of the elliptic integral and ϵ_n , ϵ_{end} ,

and ϵ_3 are the effective dielectric constant for each respective partial capacitance. Also, $K(k_x)$ function can be solved using Matlab simulation.

2.5 Overview of Tunable Microwave

Among the many ferroelectric materials, $\text{Ba}_x\text{Sr}_{1-x}\text{TiO}_3$ (BST) has been intensively investigated for tunable microwave applications such as phase shifter, oscillator, resonator, and band-pass filters due to its high tunability and low dielectric loss (or loss tangent).

Dielectric properties are different in bulk state and thin film state due to size effect⁵³. BST has high tunability and low loss tangent in ceramic bulk, but has relatively lower tunability and higher loss tangent in thin film^{42,53}.

There are several critical requirements for ferroelectric thin films to be used for microwave applications. The basic critical requirements include:

- ▶ A low dielectric loss ($\tan \delta < 0.01$) over the operating range of DC electric field (less than 10V),
- ▶ A large variation in the permittivity with applied DC electric field, 50% tunability,
- ▶ The permittivity less than 500 for impedance matching purposes,
- ▶ A low leakage current (I_L) characteristic,
- ▶ A paraelectric region, i.e., above Curie temperature, T_c ,
- ▶ A single phase with dense microstructure,
- ▶ A smooth and crack free morphology.

Tunability of materials arises because it is possible to change its dielectric constant with applied electric field, and the nonlinearity behavior of its dielectric properties with respect to applied dc voltage, and the tunable dielectric constant results in

a change in the phase velocity in the device allowing it to be tuned in real time for a particular application ⁵⁴.

2.6 Pulsed Laser Deposition (PLD)

2.6.1 Overview

Although the first experiment using PLD was conducted in 1965 by Smith and Turner, there have not been intensive researches using PLD by mid 70s. There were two main turning points to draw to attention in researches using PLD; one was electronic Q-switch development in the mid-1970s and the other was development of high T_c superconducting film using PLD system in 1987. Using short laser pulse due to electronic Q-switches brought PLD to deposit thin films by congruent evaporation and small heated volume due to shallow absorption depth in target materials. Also, since the development of the high T_c superconductor, there have been wide investigations about thin film deposition in various application areas such as high T_c superconductor, tribological coating, epitaxial growth for semiconducting, ferroelectric, ferrite, biocompatible, low K dielectric, polymer deposition, superlattice films⁵⁵⁻⁶¹.

PLD methods have the many advantages compared to other deposition techniques to grow oxide thin films. These advantages are:

- ▶ High pressure operation with reactive gas such as oxygen, nitrogen, hydrogen, and ozone,
- ▶ Ability to grow complex oxide thin films more than ternary compounds,
- ▶ Possibility to transfer same chemical formula of target material to a thin film except some of volatile element such as K, Li. Need to be included excess amount in target material or usage of segmented type of target,
- ▶ Attachment of several deposition chambers in one laser system,

- ▶ Possible to grow a wide range of thin film and multilayer structure,
- ▶ Low cost operation to get similar quality like MBE grown film,
- ▶ Controlling growth rate,
- ▶ Achieving abrupt interface,
- ▶ Flexibility, fast response, energetic evaporants, and congruent evaporation.

However, PLD is not a perfect method to grow thin films. PLD also has some disadvantages. Micro-size particulates are commonly observed on the film surface due to splashing, which occurs during laser and target interaction (chapter 2.6.4.). Also, it is difficult to deposit a large area of film due to a small angular distribution of the plume.

2.6.2 PLD system configuration

PLD systems consist of three main parts: laser, optics, and deposition system. The laser is generated using electrical pumping with KrF gas mixture. The collimated laser beam is emitted with 20ns pulse duration out of the excimer laser system. Then through several paths such as reflect mirrors and focusing lens, this laser beam goes into the deposition chamber, and then reacts with the target material. This reaction causes plume, which is directed to the substrate surface. Finally, it deposits a thin film on the substrate surface.

2.6.2.1 Laser (Light Amplification by Stimulated Emission of Radiation)

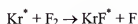
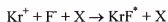
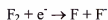
The range of laser wavelength, which is used to grow thin films by PLD is mostly between 200nm and 400nm. In this region most of the materials used for PLD show strong absorption. Absorption coefficients increase as the wavelength approaches 200nm, and the penetration depths into the target materials relatively decrease. Therefore, using closed to 200nm of laser wavelength is favorable due to ablation of thin layer of target

surface, and the stronger absorption at the short wavelength lowers the threshold of ablation.

Unlike $\text{Nd}^{3+}:\text{YAG}^{62}$, a solid state system, the excimer is a gas laser system. The excimer lasers emit their radiation directly in the UV range, without modifying their frequency. High outputs more than 1J/pulse, and pulse repetition up to several hundred Hz with energies near 500mJ/puls are available in the excimer laser system. Table 2-2 gives a list of excimer wavelengths of commercially used laser systems. Among the excimers listed, KrF and XeCl have been intensively used for PLD. KrF is the highest gain system for electrically discharged pumped excimer laser even though KrCl has a shorter wavelength than KrF.

In an excimer laser, lasing action takes place between an upper bound electronic state and weakly bound ground state. The excimer molecules can dissociate rapidly (vibrational period $\sim 10^{-13}$) by emitting photons spontaneously while transferring from upper to ground state. The excimer molecules have a high ratio of upper state lifetime to lower state lifetime. In other words, the excimer molecules are a good laser medium due to population inversion and high gain⁶³.

The formation of the excimer molecules are complex and can consist of several steps. Here are some of the important reactions for excimer molecules of KrF:



The * represents an electronically excited species and X is a third body (He, Ne).

Table 2-2. Excimer laser operating wavelength

Excimer	Wavelength (nm)
F ₂	157
ArF	193
KrCl	222
KrF	248
XeCl	308
XeF	351

Here are the requirements for lasing with output energies of several hundred millijoules per pulse: an order of $10^{15}/\text{cm}^3$ of population density, several $10^{23}/(\text{cm}^3 \text{sec})$ of excimer producing rate, 2 to 4 atmosphere of total gas pressure within the discharge volume, current density of 10^3 A/cm^2 , 1200K of electron temperature, and discharge field strength of 10-15kV/cm (this limits the spacing of discharge electrode to 2 -3 cm) are required.

Rare gas (Xe, Kr), halogen (He, F), and Ne as a buffer gas are used for excimer laser. Operating pressures are around 3000mbar and the total volume of gas required is approximately 125 – 200 liters. Usually, working gas lifetime is estimated to 2 million laser shots per fill. However, gas lifetime depends on the wavelength of the laser. As the wavelength of the laser used decreases, the gas lifetime also decreases due to a large absorption cross-section of impurities present.

Figure 2-12 shows the schematic diagrams of photon interaction to produce the laser. When atom falls to the ground state from the excited state energy level, photon is

emitted. This photon should collide with another atom, which has another electron in the same excited state, to cause stimulated emission. In this way, once emitted photon can stimulate or induce atomic emission so that the emitted photon vibrates with the same frequency and direction of previous photons.

Lasing material is contained in a long narrow container called the cavity. It is necessary to have a pair of mirrors at either end of the cavity to produce the laser. These mirrors are often known as an optical oscillator due to the process of oscillating photons between the two-mirrored surfaces. The mirror positioned at one end of the optical oscillator is half-silvered, therefore it reflects some light and lets some light through. Photons traveling at an angle will be absorbed by the cavity wall, but photons traveling parallel to the cavity axis will be allowed to pass through the half-silvered mirror. This is the light that is emitted from the laser. During this process photons are constantly stimulating other electrons to make the downward energy jump, hence causing the emission of more and more photons and an avalanche effect, leading to a large number of photons being emitted of the same wavelength and phase⁶⁴. This laser beam is monochromatic, coherent and highly directional.

2.6.2.2 Optics

Optics consist of reflecting mirror, beam splitter, focusing lens, and laser window. The reflecting mirror makes the laser system able to have several deposition chambers by changing the beam path 90°. Beam splitters split the laser beam into two or more separate beams. Focusing lens converge the laser beam into a small beam size. Laser windows have high transmittance of the incident laser beam. Therefore, these optics need to be very flat (1/8 to 1/20 wave) and free of defects. Table 2-3 shows laser window and lens materials, and their transmittance.

Table 2-3. Transmittance range for various lens and window materials

Materials	Transmittance range (nm)
Magnesium fluoride	140 – 7500
Sapphire	150 – 5000
Calcium fluoride	150 – 8000
UV-grade fused silica	190 – 2500, 2600 – 4000
Borosilicate crown glass	315 – 2350
Zinc sulphide	400 – 12,000
Zinc selenide	550 – 16,000

2.6.2.3 Deposition System

The laser beam through optics enter deposition system. This laser beam is focused to the target, which is ablated to deposit film on the substrate placed opposite side of target. The deposition system also consists of several parts such as chamber, target manipulate, substrate holder and heater, mass flow controller, and vacuum gauges. Figure 2-13 is the schematic diagram of the deposition system.

2.6.3 Laser and Target Interaction (Phenomena inside deposition chamber)

There are two mechanisms that occur when the laser beam and target material interact. The first is a primary mechanism, which can be categorized into collision, electronic, exfoliation, and hydrodynamic sputtering. The second is a secondary mechanism, which can be categorized into outflow with reflection, effusion with reflection, and effusion with recondensation. These primary mechanisms are briefly reviewed here ⁶³.

Collisional sputtering. Collisional sputtering, which is known as a momentum transfer in direct laser beam-surface interactions cannot occur with laser pulses. However, indirect collisional sputtering occurs if plasma forms during the interaction between the laser beam and the target surface.

Thermal sputtering. Thermal sputtering can occur with laser pulses due to vaporization from the surface of a heated target. The temperature of vaporized area of target surface may be much higher than melting or boiling points of target materials.

Electronic sputtering. Electronic sputtering is not a unique process. There are two cases in which electronic sputtering can occur. One is for high laser pulse energies, and the other is for low laser energies. For high laser pulse energies, dense electron excitation can be expected. These dense electrons will increase the total energy of each atom by an amount similar to $n_c E_{gap} / n_c$, where E_{gap} is the energy gap of the target material. For low laser pulse energies, defects formed in and near the surface including self-trapped excitons, can lead to the energetic expulsion of individual atoms.

Exfoliation sputtering. Exfoliation sputtering occurs by repeated thermal shock of target material. Flakes are detached from the target material. This is expected to occur when target materials have a high linear thermal expansion. This repeated thermal shock causes a crack on target materials. The thermal stress of a material is a measurement of thermal shock.

$$\text{Stress} = E\Delta L/L_0$$

where $\Delta L/L_0$ is a linear thermal expansion (L_0 is the thickness that heated, and ΔL is the changed in thickness), and E is Young's modulus.

Hydrodynamic sputtering. Hydrodynamic sputtering is a process, which droplets of material are formed and expelled from a target as a consequence of the transient melting.

When the laser beam is incident to the target, the laser beam is absorbed on the target. There are three main absorptions : first, volume absorption by electrons and phonons in the lattice, second, absorption by free carriers on target surface, and third, absorption by plume.

As the laser beam is reacted with target materials, molten layer, which is known as Knudsen layer, is formed by absorbing the photon. This molten layer which exists a short time is vaporized by exerting the plume, which consists of ions, molecules, electrons, atoms, and micro-size particulates.

2.6.4 Origin of Splashing

Splashing is one of two main drawbacks of PLD. Splashing usually occurs in most materials except for those high vapor pressures at a temperature much below the melting temperature such as CdTe and II-VI compounds, dense and single crystal targets, and targets with high thermal conductivity. At least three mechanisms--subsurface boiling, expulsion of liquid layer, and exfoliation--are involved in depositing particulates on surface during PLD growth.

Subsurface boiling. Subsurface boiling, also known as true splashing occurs when the subsurface layer is molten first before the surface layer⁶⁵. This process ejects micro-sized molten droplets onto the substrate. By reducing the deposition rate with laser power, this splashing caused by boiling the subsurface can be reduced. Schwarz and Tourtellotte⁶⁶ calculated the maximum power density, which could be absorbed on a solid surface without causing splashing.

$$D_{\max} = L\rho H_{ev} / t_r$$

where t_r is the relaxation time, L is the range of surface penetration of the light intensity into the solid of mass density, ρ , and the heat of evaporation, H_{ev} .

Expulsion. Expulsion of the liquid layer comes from above the liquid layer in a form of recoil pressure exerted by the shock wave of the plume. This mechanism is difficult to distinguish with true splashing. This one also can be reduced by lowering laser power density with reduced deposition rate.

Exfoliation. Exfoliation is caused by target morphology, which is affected by repetitive ablation with laser beam. This repetitive ablation forms long needle-shaped microstructures on target surface. These needle shaped microstructures, which is directed to the incoming laser beam due to a shadowing effect, are very fragile and can be easily broken by the thermal shock induced during the intense laser irradiation. These broken microstructures are incorporated into the plume and then deposited on the substrate.

To avoid particulate deposition by splashing, several ways have been considered. One is the use of a mechanical particle filter, which can remove slowly moving particles by placing the high velocity pass filter between the substrate and target. Second method includes manipulating the laser-target interaction geometry. Third one is using a high density target with smooth surface. This is a more effective solution to reduce the splashing. It is important to fabricate a target with more than 85 % of the theoretical densities, and high homogeneity.

The laser beam ablates one specific focused area of target. It causes non-uniform erosion of the target. To achieve uniform target erosion and consumption, the target materials need to be rotated during deposition. This rotation makes the angular ablated

track on the target. Another way is to raster the laser beams on the target surface.

However, this method has the disadvantage of moving the plume position relative to the substrate. For more than 1cm x 1cm size substrates, uniform coatings are obtained for all surface area. Finally, the target surface needs to be polished before each run.

2.6.4 Background Gas Effect

PLD is a highly recommended deposition technique to grow oxide films because of being operated under high oxygen gas pressure compared to other deposition techniques such as sputtering, MBE, and e-beam evaporation. High background gas pressure causes the several effects as follows: (1) an increase in fluorescence from all species due to collisions on the expansion front and subsequent inter-plume collisions; (2) a sharpening of the plume boundary, indicative of a shock front; (3) a slowing of the plume relative to the propagation in vacuum, resulting in (4) spatial confinement of the plume⁶³.

2.7 Defect Chemistry

Most solids have defects such as vacancies, interstitials, impurities, dislocations, grain boundaries, and cracks. Understanding these defects in oxide materials is very important because the properties of most materials are affected by defects. Among the defects such as point, linear, and planar defects, point defects will be mainly reviewed here. The following categories fall into point defects⁴⁸: Stoichiometric defect such as Schottky defect (cation-anion vacancy pair) and Frenkel defects (cation vacancy–cation interstitial pair or oxygen vacancy–oxygen interstitial pair), non-stoichiometric defects such as oxygen deficiencies or excess cation resulting from an imbalance in chemical formula of materials, and extrinsic defects such as impurities or intentional doping in a host material shown in Figure 2-14.

The following notations (Kroger-Vink notation) are used in defect chemistry.

V	for vacancy
i	for interstitial
x	for zero effective charge
'	for negative charge
·	for positive charge

The formation of point defects must follow three rules for a chemical reaction.

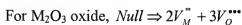
Mass balance : can not be created or destroyed

Electroneutrality or charge balance : can not be created or destroyed

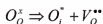
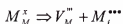
Preservation of regular site ratio : the ratio between the number of cation and anion sites must remain constant and equal to the ratio of the parent lattice

Schottky, and Frenkel defect reactions are representative reaction in case of stoichiometric defect.

In Shottky defect reaction, the following reaction occurs:

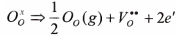


For Frenkel defect reaction



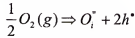
Nonstoichiometric defect reactions cause the change in composition of the crystal.

Mass is transferred across the boundaries of the crystal. There are several cases that cause a nonstoichiometric defect reaction. One case occurs at low oxygen partial pressure. The net Reaction is



Oxygen vacancies are doubly ionized and carry an effective charge of +2. Also, this reaction leaves two weakly bound electrons, which can be easily excited into the conduction band.

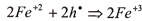
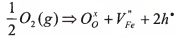
A second case is when oxygen is incorporated into the crystal interstitially:



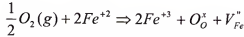
In this case, ionization can also occur and create holes in the valence band; the defect acts as an acceptor.

The third case is when the oxidation state of the cations in the transition metal is changed.

For oxidation of Fe_3O_4 , which is spinel structure,



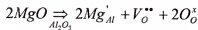
for a net reaction on above two reactions



This reaction creates holes to change the valence state of the cation from +2 to +3.

There is no existence of 100% pure material. Crystals even known as pure crystal contain impurities. These impurities are placed into crystals substitutionally or interstitially.

Let us think about MgO doping into Al_2O_3 first, which is p-type doping.



second, Al_2O_3 doping into MgO , which is n-type doping.



2.8 Characterization

2.8.1 X-Ray Diffraction (XRD)

X-ray diffraction is one of the basic characterization tools to identify crystalline qualities and phases of crystals in bulk materials and thin films. Also, structural properties such as strain, grain size, epitaxy, phase composition, preferred orientation, and defect structure can be measured using XRD.

For a cubic system, a distance (d_{hkl}) between planes can be obtained from the lattice constant (a_0), and Miller indices of plane ($h\ k\ l$).

$$d_{hkl} = \frac{a_0}{\sqrt{h^2 + k^2 + l^2}}$$

The thin films (or bulks) are exposed to a monochromatic beam ($\lambda = 1.5404$) of x-rays from a $\text{Cu-K}\alpha$, and incident x-rays on a sample are scattered in all directions. However, when there is constructive interference in certain direction after x-rays are scattered by the atomic planes in a crystal, a diffraction peak is observed. The condition for constructive interference from planes with spacing d_{hkl} is given by Bragg's law.

$$n\lambda = 2d_{hkl} \sin \theta_{hkl}$$

where θ_{hkl} is the angle between the incident x-ray beam and the atomic planes (Figure 2-15). For diffraction to be observed, the detector must be positioned so the diffraction angle $2\theta_{hkl}$, and the crystal must be oriented so that the normal to the diffraction plane is coplanar with the incident and diffracted x-rays, and so that the angle between the diffracting plane and the incident x-rays is equal to the Bragg angle θ_{hkl} . For a single

crystal or epitaxial thin film, there is only one specimen orientation for each (hkl) plane where these diffraction conditions are satisfied.

2.8.2 Four Circle XRD

For the thin film and single crystal x-ray diffraction, a four-circle x-ray diffractometer is used. By using the four circles of the diffractometer, the sample can be oriented at different angles to the incident beam so that different crystallographic planes contribute to diffraction^{67,68}. Figure 2-16 shows the geometry of sample for four circle XRD. The sample can also be rotated about its normal, and from the number of diffraction peaks obtained over a 360° scan the symmetry of the sample surface can be studied. Thus, the complete 3D crystal structure and orientation of the thin film with respect to the substrate can be determined. Using a four-circle diffractometer like one shown in Figure 2-16, one can determine the in-plane and out-of-plane lattice parameters, as well as domain structure and crystalline quality through a variety of scans such as normal θ -2 θ scans, rocking curves, off-axis ϕ scans, and grazing incidence scans.

In the off-axis ϕ scans, the q vector is at an angle to the plane of the film. As the sample is rotated about the ϕ -axis over 360°, this scan reveals information regarding the symmetry of the crystal structure of the sample. The crystallographic domain structure and epitaxy of the film can be characterized.

2.8.3 Atomic Force Microscopy (AFM)

AFM is one of the powerful techniques to image a surface of a material with nano-scale resolution in all three dimensions unlike SEM (Scanning Electron Microscopy). Sample preparation for AFM is simple compared to SEM or STM (Scanning Tunneling Microscopy). This means almost any surface of materials can be

studied using AFM including insulators, semiconductors, conductors, and transparent materials. In addition, AFM is a non-destructive technique, which does not require coating of a conducting layer on the surface of materials.

AFM uses a sharp tip mounted on a flexible cantilever. When the tip comes within a few Å of the sample's surface, repulsive van der Waals forces between the atoms on the tip and those on the sample surface cause the cantilever to deflect. The magnitude of the deflection depends on the tip-to-sample distance d . For AFM, there are two modes to image the surface. One is contact mode, which the tip moves on the surface, and the other is tapping mode, which the tip vibrates on the surface. Usually, tapping mode is used to image a soft surface like polymers.

Figure 2-17 shows the schematic diagram of AFM. The deflection of the tip is monitored using a laser beam and position-sensitive photodiode (PSPD). Light from a laser diode is reflected from the back of the cantilever into the PSPD. A given cantilever deflection will then correspond to a specific position of the laser beam on the PSPD. Because the PSPD is very sensitive (about 0.1Å), the vertical resolution of AFM is sub-Å. AFM gives information such as topography, profilometry, roughness of surface, and grain size.

2.8.4 Transmission Electron Microscopy (TEM)

TEM has a high lateral resolution better than 0.2nm , and gives both image and diffraction information from a single sample. High voltage TEM has an advantage than low voltage TEM in terms of electron penetration depth with less scattering. This makes it possible for TEM to use thicker samples. Electron penetration is determined by the mean distance between electron scattering events. There is also a disadvantage using TEM. That is its limited depth resolution because even though electron scattering occurs

in three dimensions, electron scattering information is projected on to a two dimensional fluorescent screen. Sometimes to overcome this poor depth resolution, samples are tilted.

TEM gives two ways of sample observation, diffraction mode and image mode. In diffraction mode, an electron diffraction pattern is obtained on the fluorescent screen, originating from the sample area illuminated by the electron beam. The diffraction pattern is equivalent to an X-ray diffraction pattern. A single crystal produces a spot pattern, a polycrystal produces a powder or ring pattern, and a glassy or amorphous produces a series of diffuse halos. The image mode produces an image of the illuminated sample area instead of a diffraction pattern. The image can contain contrast brought about by several mechanisms: mass contrast due to spatial separations between distinct atomic constituents; thickness contrast due to nonuniformity in sample thickness; diffraction contrast which in case of crystalline materials results from scattering of the incident electron wave by structural defects; and phase contrast.

2.8.5 Hall measurement

To measure Hall properties of samples, the van der Pauw geometry is chosen. The resistivity of the sample can be measured without patterning, regardless of the shape of the sample. Figure 2-18 shows a configuration of four wires for the van der Pauw methods to measure resistivity and Hall voltage⁶⁹. The resistance R_1 is measured as the voltage output between contacts 1 and 2 per unit current through 3 and 4. Also, R_2 is measured as same way of R_1 by current on 2 and 3 and voltage on 1 and 4. The resistivity of the sample is obtained by the equation

$$\rho = \frac{\pi d}{\ln 2} \frac{(R_1 + R_2)}{2} f\left(\frac{R_1}{R_2}\right)$$

Hall constant is measured by applying a magnetic field normal to the sample and current on the sample surface perpendicular to the magnetic field shown in Figure 2-18(c).

The number of conduction electrons (per unit volume)

$$N = -\frac{j_x B}{e \varepsilon_y}$$

Hall constant, R_H , is inversely proportional to the density of charge carriers, N .

$$R_H = -\frac{1}{Ne}$$

R_H is negative when electrons are the predominant charge carriers.

2.8.6 Capacitance and Voltage Measurements

Capacitance versus voltage measurements give useful electrical information for oxide samples. Agilent HP 4284A was used to measure the dielectric properties such as capacitance, and loss tangent of oxide thin films on substrates. Frequency can be applied from 20Hz to 1MHz while a bias voltage ranging from -40 and 40V is applied with a small ac signal on the electrodes.

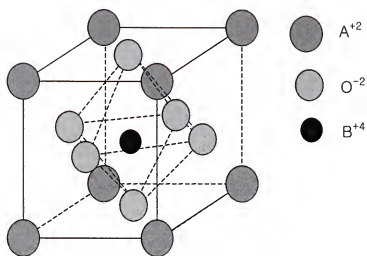


Figure 2-1. Perovskite structure

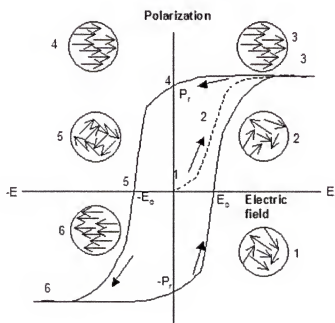


Figure 2-2. Ferroelectric hysteresis loop

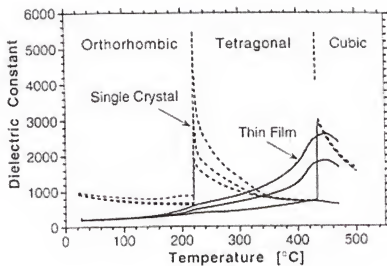


Figure 2-3. Dielectric constants as a function of temperature for KNbO_3 ⁴¹

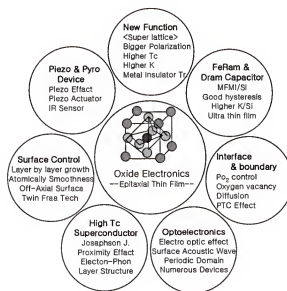


Figure 2-4. Application fields and fundamental technical terms in future oxide electronics

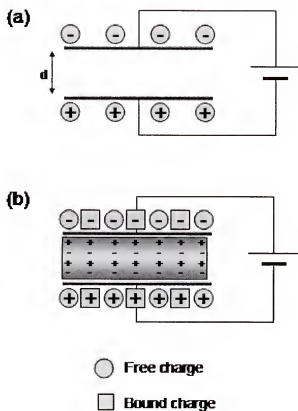


Figure 2-5. Schematic diagrams of (a) Parallel plate capacitor of area A and separation d in vacuum attached to a voltage source and (b) parallel plate capacitor with dielectric material between two plates

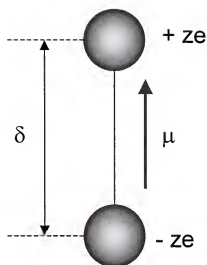


Figure 2-6. Definition of electric dipole moment

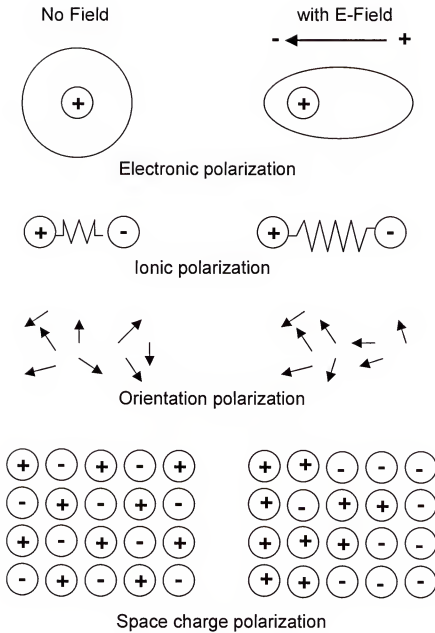


Figure 2-7. Schematic representation of different mechanisms of polarization ⁴⁷

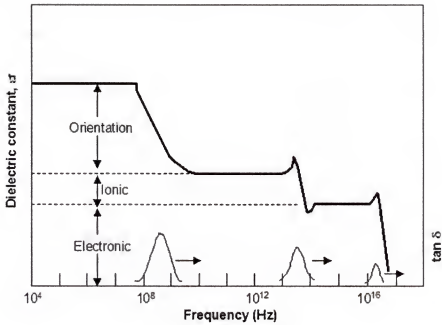


Figure 2-8. Frequency dependence of several contributions to the polarizability

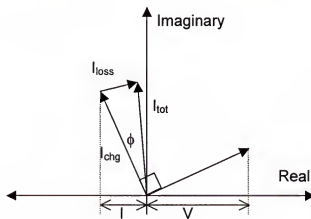
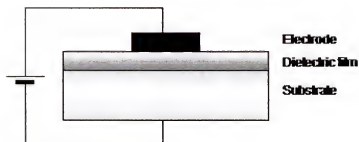


Figure 2-9. Applied voltage, charging, loss, and total currents for a capacitor

Parallel Plate Capacitor



Coplanar slot capacitor



The split dielectric resonator

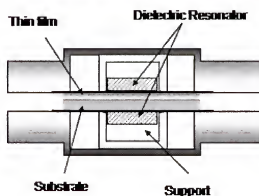


Figure 2-10. Schematic diagram of several capacitor measurement techniques

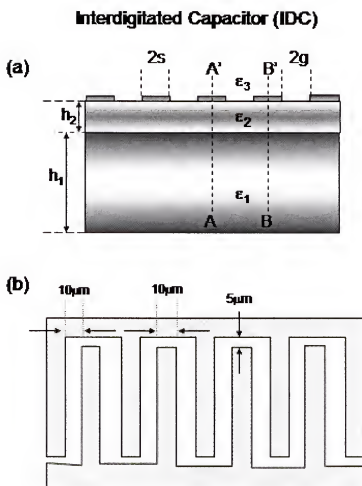


Figure 2-11. Schematic diagram of (a) Interdigital capacitor (IDC) structure and (b) top electrodes

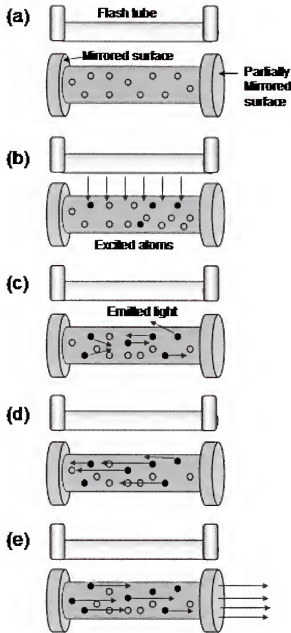


Figure 2-12. Schematic diagrams of photon interaction to produce laser; (a) non-lasing State, (b) excitation of atoms using light source, (c) photon emission, (d) stimulated emission of further photons, and (e) column of laser light leaving optical oscillator

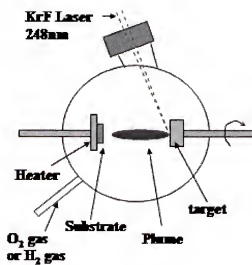


Figure 2-13. Schematic diagram of pulsed laser system (PLD)

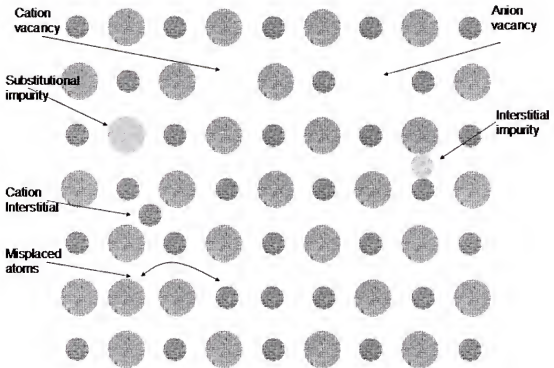


Figure 2-14. Various type of defects typically found in ceramics. Misplaced atoms can only occur in covalent ceramics due to charge considerations

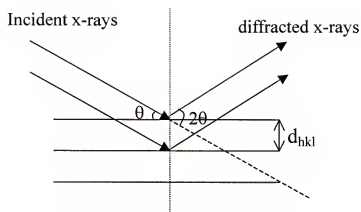


Figure 2-15. Bragg's law

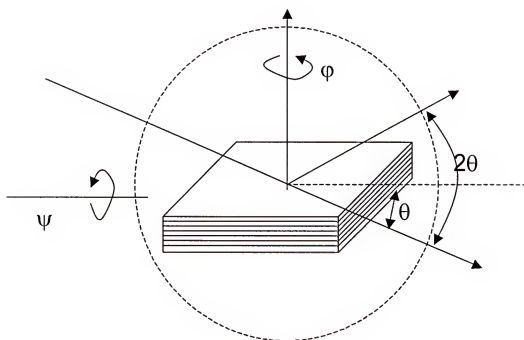


Figure 2-16. Geometry of four circle x-ray

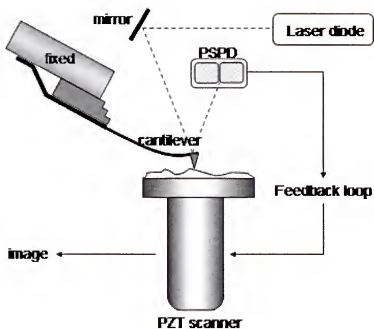


Figure 2-17. Schematic diagram of atomic force microscopy

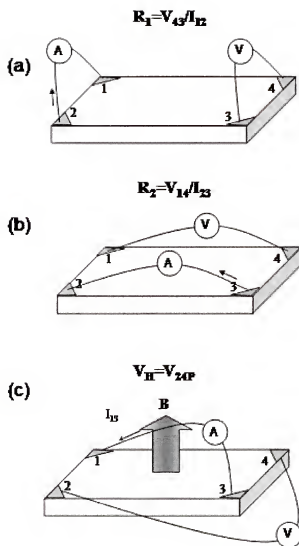


Figure 2-18. Schematic diagram of the geometry of Van der Pauw measurements; (a) resistivity, and (b) Hall constant, R_H

CHAPTER 3

SURFACE TREATMENT FOR FORMING UNIT-CELL STEPS ON THE (001) KTAO₃ SUBSTRATE SURFACE

3.1 Introduction

Perovskite thin-film materials display a variety of interesting properties, including magnetoresistance⁷⁰, superconductivity⁷¹⁻⁷⁴, optical nonlinearity⁷⁵, large dielectric polarizability, and magnetism. Many of these properties are potentially useful for thin film device applications. In most cases, the crystalline quality of epitaxial thin films determines the utility of the material for devices of interest. In all cases, the crystallinity of the film depends on the properties of the substrate surface. For the epitaxial growth of thin films with minimal defects, the surface of the substrate should ideally be atomically flat, thus facilitating the growth of films via layer-by-layer or step-flow growth modes.

Studies of surface treatments that yield unit cell steps on perovskite single crystal substrates have been limited in scope, with most activity focused on the (001) SrTiO₃ surface^{24,25,76-83}. Surface with unit-cell steps can be used to grow quantum wires or superlattices. Using atomic force microscopy (AFM) or scanning tunneling microscopy (STM), it has been shown that producing a (001) surface on SrTiO₃ with unit-cell steps is possible via a conversion of the surface to strontium hydroxide, etching the hydroxide layer with buffered HF (BHF), and then following this etch with a high temperature anneal. Using this approach, a TiO₂-terminated SrTiO₃ surface is realized. In a A⁺²B⁺⁴O₃ compound, the sub-units (SrO and TiO₂) are charge neutral, which apparently plays a role in the stability of either a TiO₂ or SrO termination. While SrTiO₃ has previously received

a significant level of attention, there have been only a limited number of studies of surface treatments for other perovskites with different cation valences. KTaO_3 is a prototypical $\text{A}^{+1}\text{B}^{+5}\text{O}_3$ cubic perovskite that displays interesting optical and dielectric properties^{42,46,84}. It has a cubic lattice parameter $a = 3.9885\text{\AA}$ and has been characterized previously as a substrate for the epitaxial growth of various oxide thin films⁸⁵⁻⁹⁰. The dielectric constant of KTaO_3 is 4500 (at 200 kHz and 4.2K) and the loss tangent is 0.001. In the present work, surface treatments employing wet chemical etching and annealing have been carried out for a polished KTaO_3 substrate with the objective of achieving epitaxial-quality (001) surfaces with unit-cell steps. In the future, quantum wires and superlattices can be grown on the surface treated KTaO_3 substrates having unit-cell steps.

3.2 Experimental Methods

The substrate surfaces were initially prepared by the chemical-mechanical polishing of (100)-oriented KTaO_3 single crystals. The substrates were then ultrasonically cleaned using trichloroethylene, acetone, and methanol, followed by drying with an N_2 gas flow. As shown in the AFM image in Figure 3-1, the as-polished surface did not exhibit any evidence of a step structure, and the RMS roughness was determined to be 0.238nm. The evolution of the surface structure on KTaO_3 substrates initially prepared as described above was examined for samples that were subsequently etched with a commercially available buffered oxide etchant (BOE) (i.e., $\text{NH}_4\text{F}:\text{HF} = 7:1$) followed by annealing treatments in air. The surface morphology of the etched/annealed (100) KTaO_3 surfaces was then characterized using a Digital Instruments Nanoscope III AFM operating in air in the contact mode.

3.3 Results and Discussion

The surface chemistry of KTaO_3 is similar to that of SrTiO_3 in that the *A*-site termination is expected to yield a stable hydroxide termination when exposed to air. Accordingly, as in the case of SrTiO_3 , the formation of unit-cell-high steps on the (001) KTaO_3 surface via hydroxide removal by etching followed by annealing treatments was explored. Surfaces that were annealed with no etching treatment yielded no step structure. Figure 3-2 shows the surface microstructure of a KTaO_3 (001) crystal that was not etched but that was subjected to annealing at 900 and 1000°C. No step structure evolves after annealing at temperatures up to 1000°C for extended times (up to 4 h). The lack of surface steps is attributed to a failure to remove the hydroxide termination. If the (001) KTaO_3 substrate is first etched in the buffered-oxide etchant and then annealed at high temperature, unit-cell-high steps are observed as can be seen in Figure 3-3. For the surface shown in Figure 3-3, the substrate was etched at room temperature for 15 min and then annealed in air at 700°C for 3h. The height of the steps varies between ~4 to 6 Å and ~12 Å. Previous work on the (001) KTaO_3 surface suggests that a segregation of K occurs as the single crystals are subjected to high temperature annealing, with the possible formation of Ruddlesden-Popper type $\text{KO}(\text{KTaO}_3)_n$ phases near the surface⁹¹. This effect could explain the observed step heights of ~6 Å and ~12 Å.

The formation of a stepped surface microstructure on KTaO_3 was sensitive to the specific etching/annealing treatment applied. Figure 3-4 shows AFM images of KTaO_3 surfaces that were etched in BOE for various times followed by annealing at 700°C for 4 hours. These images are 5µm x 5µm in size. For a 12 min etch, there is no significant change in the KTaO_3 surface structure after annealing - as is evident in Figure 3-4 (a).

However, for a slightly longer etch time, surface steps do emerge. For the surface shown in Figure 3-4 (b), the etching time was 15 min. The height of the surface steps of approximately 0.4 nm is agreement with the lattice parameter of KTaO_3 . The width of the terraces for this sample was 500-800 nm. This yields a miscut angle for the (001) KTaO_3 crystal of less than 1° . It should be noted that, if the etching time is extended beyond 15 min, macroscopic particles are observed to form on the surface following the annealing step. Figure 3-4 (c) shows the surface of a substrate that is etched for 30 min then annealed at 700°C for 4 hours. The precipitates are sub-micron in diameter. The RMS roughness of the substrates as a function of etching time for samples annealed at 700°C for 4 h is shown in Figure 3-5.

The resulting surface structure for samples subjected to higher temperature anneals was also examined. Figure 3-6 shows the AFM images of KTaO_3 surfaces that were etched for various times with BOE, then annealed in air at 900°C for 4 hours. Figure 3-6 (a) shows a surface that was annealed without etching. No etch pits were observed in the KTaO_3 surfaces, as are often observed for (001) SrTiO_3 . As can be seen in Figure 3-6 (b), a step structure begins to appear on the surface of KTaO_3 when etched for 2 min, followed by annealing at 900°C . This is more clearly seen in Figure 3-7. With 5 min of etching (Figure 3-6(c)), round particulates become evident after annealing. The size of these particles is 80 – 160 nm. These particulates are believed to be Ta_2O_5 that forms due to a loss of K from the KTaO_3 surface during annealing. Previous thermogravimetric measurements on KTaO_3 crystals annealed at $800\text{--}900^\circ\text{C}$ indicated that some depletion of the material due to K loss does occur [27]. We were unable to verify the composition of these particulates due to their relatively small size. Figure 3-8

shows the RMS surface roughness results for a (001) KTaO_3 crystal etched at various times, followed by annealing at 900°C . The RMS values increased as etching time increased. Note that the surface roughness of KTaO_3 annealed at 700°C is smaller than for samples annealed at 900°C . Figure 3-9 shows AFM images of KTaO_3 single-crystal surfaces annealed in air at 1000°C for 1 hour ($5\mu\text{m} \times 5\mu\text{m}$ in image size) both: (a) without and (b) with chemical etching. The surface roughness of the annealed KTaO_3 substrate without etching was larger than that of other substrates etched for different times. No particulates were observed on the surface even though the annealing temperature was the highest employed.

Although unit-cell-high surface steps could be formed for (001) KTaO_3 substrates etched in BOE, followed by annealing in air, the volatility of K from the surface during the anneal remains a concern. In order to address this issue, several etched substrates were annealed in a covered crucible that contained the substrate and additional KTaO_3 powder. The KTaO_3 powder provides an over pressure of K and should reduce the K loss. Figure 3-10(a) shows AFM images of KTaO_3 (001) single crystals that were etched with BOE, followed by annealing at 700°C for 3 hours in air either with or without the presence of KTaO_3 powder. The KTaO_3 surface in Figure 3-10(a) was etched with BOE for 18 min, then annealed at 700°C for 3 hours with KTaO_3 powder. In this image, particles are observed on the surface of KTaO_3 . Figure 3-10(b) shows AFM images of KTaO_3 single crystal surfaces after etching with BOE for 8 min and then annealing in air at 1000°C for 3 hours with KTaO_3 powder. In this case, the particulates are not randomly oriented on the surface, but are aligned along either the $[100]$ or $[010]$ directions. The average height of the particulates is ~ 30 nm and their width is around 200 nm. Again, it

is difficult to determine the composition of these particulates due to their small size. The RMS value of a $10\text{ }\mu\text{m} \times 10\text{ }\mu\text{m}$ area of the substrate was 4.980 nm and the RMS value of the particle-free region was 0.580 nm.

3.4 Conclusion

The formation of unit-cell-high steps on a (001) KTaO_3 surface was achieved. The two-step process (etching and annealing) for forming unit-cell steps suggests that the as-polished substrates have a surface terminated by a hydroxide, presumably potassium hydroxide. The etching step removes the hydroxide, yielding a surface suitable for reconstruction via annealing. Longer etching times and higher annealing temperatures cause a roughening of the surface and the formation of particulates on the surface of the KTaO_3 (100) face.

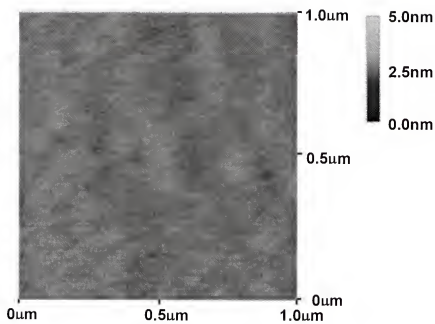


Figure 3-1. AFM image of a chemically-mechanically polished KTaO_3 surface.

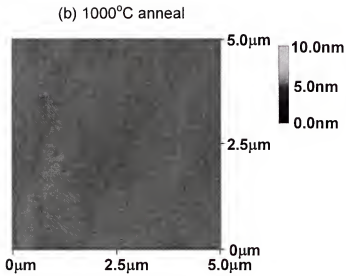
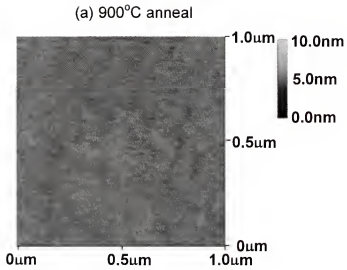


Figure 3-2. AFM images of a KTaO_3 surface that was: (a) annealed at 900°C for 4h, and (b) annealed at 1000°C for 4h.

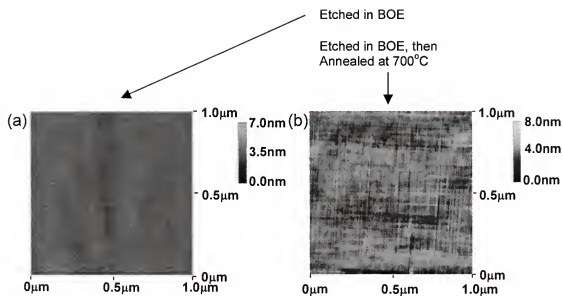


Figure 3-3. AFM images of a KTaO_3 surface that was: (a) etched 18min only, and (b) etched 15min, then annealed 700°C for 3h.

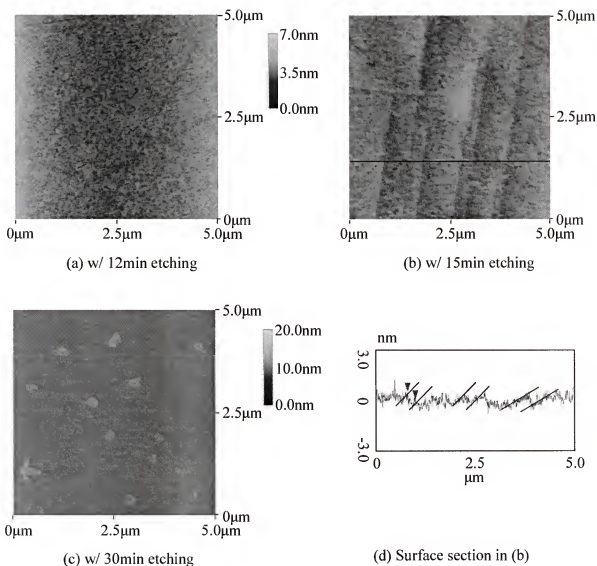


Figure 3-4. AFM images of surface-treated KTaO_3 as a function of etching time with BOE and then annealed at 700°C for 4 h: (a) 12 min, (b) 15 min, (c) 30 min ($5\mu\text{m} \times 5\mu\text{m}$), and (d) surface section in (b).

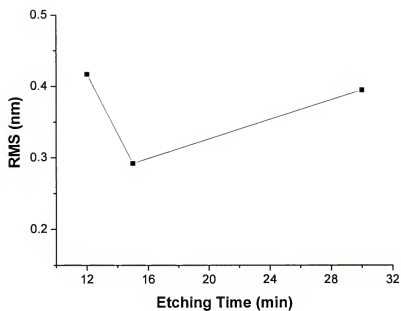


Figure 3-5. RMS surface roughness values of surface-treated KTaO_3 as a function of etching time with BOE and then annealed at 700°C for 4 h.

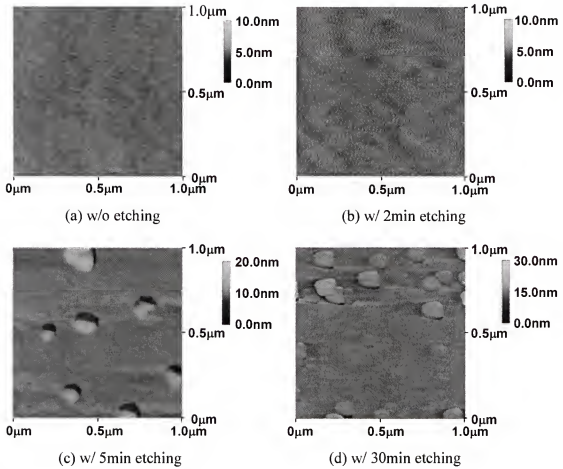


Figure 3-6. AFM images of surface-treated KTaO_3 as a function of etching time with BOE and then annealed at 900°C for 4 h : (a) without etching, (b) 2 min, (c) 5 min, and (d) 30 min ($1\mu\text{m} \times 1\mu\text{m}$)

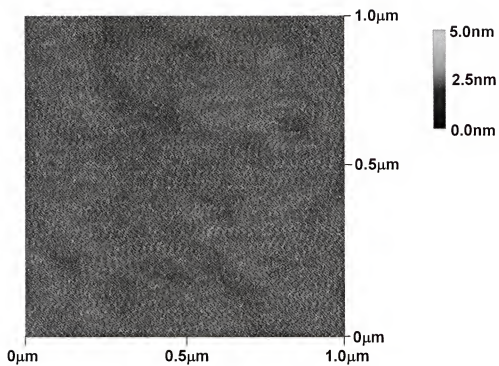


Figure 3-7. Enlarged AFM image of KTaO_3 etched with BOE for 2 min followed by annealing at 900°C ($1\mu\text{m} \times 1\mu\text{m}$)

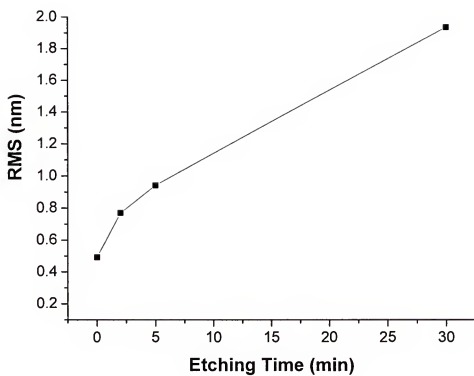


Figure 3-8. RMS surface roughness values of surface treated KTaO_3 as a function of etching time with BOE and then annealed at 900°C for 4 h.

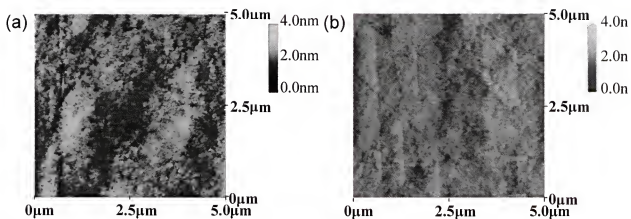


Figure 3-9. AFM images of a KTaO_3 single crystal surface annealed at 1000°C for 1 h (a) without etching and (b) after etched in BOE for 10 min.

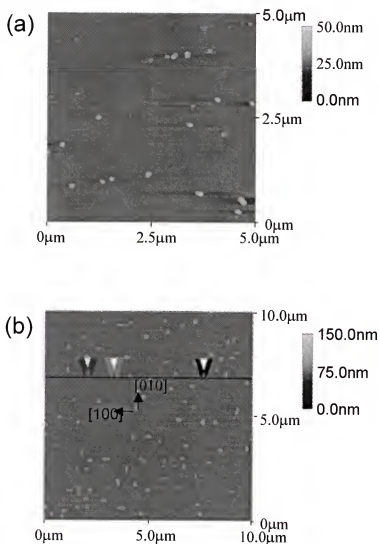


Figure 3-10. AFM images of a KTaO_3 single-crystal surface that was (a) etched in BOE for 18 min, then annealed at 700°C for 3 h with KTaO_3 powder. The RMS roughness was 1.385 nm (RMS of particle-free area : 0.450 nm). Also shown (b) are AFM images of a KTaO_3 surface that was etched in BOE for 8 min and then annealed at 1000°C for 3 h with KTaO_3 powder. The RMS was 4.980 nm, (in the particle-free area : 0.580 nm).

CHAPTER 4 GROWTH OF SEMICONDUCTING KTAO₃ THIN FILMS

4.1 Introduction

Perovskites represent an important class of oxide materials, exhibiting many interesting properties, including piezoelectric, pyroelectric, ferroelectric, and electro-optic⁹². Many of these materials can be doped with charge carriers to yield semiconducting behavior as well. At elevated temperatures, semiconducting perovskites are useful in gas sensor and fuel cell applications^{93,94}. Recently, both metallic and semiconducting perovskites have been explored as conducting oxide electrodes in ferroelectric memory devices⁹⁵ as well as a channel material in novel electric field-effect device structures⁹⁶. Among the perovskite materials, KTaO₃ has several properties that make it attractive for study as a semiconducting thin film material. The insulating KTaO₃ system has been investigated for use in optical waveguides and tunable microwave applications. KTaO₃ is an incipient ferroelectric material with a cubic perovskite structure ($a=3.9885$ Å) and formal ionic charges of K⁺, Ta⁵⁺, and O²⁻^{42,97,98}. The dielectric constant of KTaO₃ is 4500 at 4.2K (200kHz) and 243 at 25°C (200kHz). In comparison to other perovskite materials, such as the titanates or zirconates, achieving semiconducting behavior in KTaO₃ is relatively difficult. This is due, in large part, to the strong tendency of Ta to assume the +5 oxidation state. Nevertheless, n-type semiconducting behavior has been reported in bulk material either by cation doping or through the introduction of O vacancies in reduced conditions^{99,100}. One candidate donor dopant is Ca²⁺, as substitution on the K⁺ site should yield electron doping. While pure KTaO₃ bulk crystals exhibit a

high resistivity due to the large bandgap, reduction of the crystal to KTaO_{3-x} can result in a resistivity of $10^{-1} \Omega\text{cm}$, a Hall mobility as high as $30 \text{ cm}^2/\text{Vs}$ at room temperature and $2.3 \times 10^4 \text{ cm}^2/\text{Vs}$ at 4.2K, and a carrier concentration of $10^{17} - 10^{19} \text{ cm}^{-3}$ ¹⁰¹. The bandgap of KTaO_3 is $\sim 3.8 \text{ eV}$ ¹⁰². From electron tunneling measurements, the density of states effective mass was estimated to be $0.5 - 0.7 m_e$ ^{103,104}, which is remarkably low for a semiconducting perovskite oxide.

4.2 Experimental Methods

Given these attractive semiconducting properties in bulk materials, it would be interesting to investigate the synthesis of semiconducting KTaO_3 thin films for potential semiconducting oxide applications. Numerous semiconducting perovskite materials have been grown as thin films, including cation-doped BaTiO_3 ¹⁰⁵⁻¹⁰⁷ and SrTiO_3 ^{108,109}. However, the synthesis of semiconducting KTaO_3 films has not been reported. In this paper, we examine the growth of semiconducting KTaO_3 thin films using pulsed-laser deposition. Single crystal MgO (100) was used as the substrate material. Prior to deposition, the MgO substrates were ultrasonically cleaned with trichloroethylene, acetone, and methanol, followed by compressed N_2 drying. For the growth of both undoped and 1 at. % Ca doped KTaO_3 films, segmented laser ablation targets were prepared^{41,110}. In the growth of KTaO_3 films, potassium deficiency is a significant issue due to the high vapor pressure of potassium at the deposition temperature range of 650 - 750°C. In order to compensate for potassium loss, a segmented target, consisting of 50% KTaO_3 and 50% KNO_3 , was used. Schematic diagram of the segmented $\text{KTaO}_3/\text{KNO}_3$ target was shown in Figure 4-1. Base pressure of the deposition chamber was 4.5×10^{-6} Torr. A KrF (248nm) laser was used at a frequency of 5Hz and energy density of $5\text{J}/\text{cm}^2$.

Distance between target and substrate was ~6cm. Prior to growth, the laser target was cleaned in situ by preablating with approximately 2000 shots. Film thickness was 200 nm with a growth rate of 0.11 Å/pulse. The deposited films were characterized using X-ray diffraction, atomic force microscopy, field-emission scanning electron microscopy, and Hall measurement.

4.3 Results and Discussion

Initial efforts focused on the growth of epitaxial Ca doped KTaO_3 in an oxygen background ambient. Both crystallinity and transport were studied as a function of deposition temperature and oxygen pressure. Figure 4-2 shows the X-ray diffraction results for KTaO_3 :Ca films grown in 10^{-4} Torr of oxygen at various deposition temperatures. For the 50/50 Ca doped- $\text{KTaO}_3/\text{KNO}_3$ segmented target configuration, a deposition temperature of 700 °C resulted in a high degree of crystallinity as determined by X-ray diffraction. The lack of good crystallinity for KTaO_3 :Ca films deposited at 750 °C may reflect potassium deficiency due to the high vapor pressure of potassium at this deposition temperature. Despite the inclusion of Ca as a donor impurity, the films deposited at 10^{-4} Torr were insulating and transparent with no measurable conductance.

In order to explore the doping behavior further, Ca doped films were grown at 700 °C in an oxygen ambient ranging from vacuum (5×10^{-6} Torr) to 10^{-1} Torr of oxygen. Figure 4-3 shows the X-ray diffraction results for KTaO_3 :Ca films grown on MgO substrate as a function of oxygen pressure at a deposition temperature of 700 °C. Over this entire pressure range, the epitaxial growth of Ca-doped KTaO_3 was achieved. Note that the strongest intensity (0 0 *l*) KTaO_3 peaks were observed for an oxygen pressure of 10^{-3} Torr. However, for the entire pressure range, the Ca-doped KTaO_3 films were

insulating. This result differs from that observed for other perovskites, such as the titanates, in which semiconducting behavior is observed for growth in vacuum.

In order to successfully reduce the Ca-doped KTaO_3 films and achieve semiconducting behavior, the use of hydrogen as a reactive background gas was implemented. It is well known that many oxides can be made oxygen deficient via hydrogen reduction. It is also true that hydrogen can serve as a shallow dopant in some oxides. Figure 4-4 shows the X-ray diffraction results of Ca doped KTaO_3 films on MgO (100) grown at a substrate temperature of 700°C at various pressures of 96% $\text{Ar}/4\% \text{H}_2$. For Ar/H_2 pressure up to 30mTorr, epitaxial Ca-doped KTaO_3 films were obtained.

Four-circle X-ray diffraction was used to investigate in-plane alignment of the film. Figure 4-5(a) shows the ϕ -scan results for the $\text{KTaO}_3\text{:Ca}$ film on MgO . The in-plane orientation of the film is evident via a ϕ -scan through the $\text{KTaO}_3\text{:Ca}$ (110). The film is in-plane aligned with a cube on cube epitaxial relationship to the MgO substrate. The in-plane mosaic spread was 3.7° . Figure 4-5(b) shows the out-of-plane rocking curve of $\text{KTaO}_3\text{:Ca}$ (200) peak. The full width at half maximum (FWHM) of $\text{KTaO}_3\text{:Ca}$ was 2.3° . the lattice constant of the Ca-doped KTaO_3 was 3.9885 \AA . Figure 4-6 shows a FE-SEM image of the surface morphology of semiconducting $\text{KTaO}_3\text{:Ca}$ film on (100) MgO substrate deposited at 700°C for 1hr in 30 mTorr of 96% $\text{Ar}/4\% \text{H}_2$. The grain size is approximately 100-150nm.

Semiconducting properties of $\text{KTaO}_3\text{:Ca}$ film were measured for films grown at 30mTorr of 96% $\text{Ar}/4\% \text{H}_2$ atmosphere. KTaO_3 films grown under this condition were dark blue. This dark blue color is considered to be due to formation of impurity energy level inside the band gap of KTaO_3 . The room temperature properties of the $\text{KTaO}_3\text{:Ca}$

film were investigated via Hall measurement in a Van der Pauw configuration. These measurements were performed using a 8 kG field and a measurement current of 1 mA. Also, temperature dependence of resistivity of Ca-doped KTaO_3 thin film on (001) MgO was seen in Figure 4-7. The resistivity of Ca-doped KTaO_3 film decreased as temperature increased from 180K to 300K. This behavior was consistent with semiconducting behavior. The film resistivity of the Ca-doped KTaO_3 film was $10.4 \, \Omega\text{cm}$. conductivity was n-type with a Hall mobility of $0.27 \, \text{cm}^2/\text{Vs}$ and a carrier density of $3 \times 10^{18} \, \text{cm}^{-3}$. Note that semiconducting behavior was also observed for KTaO_3 (no Ca) films grown in 30 mTorr Ar/H_2 at $700 \, ^\circ\text{C}$. This suggests that oxygen deficiency is responsible for n-type behavior in both materials.

4.4 Conclusion

In this study, conditions for growth of insulating and semiconducting $\text{KTaO}_3\text{:Ca}$ film were investigated. Unlike other perovskites, such as the titanates, semiconducting behavior is not observed for growth in vacuum. This resistance to forming free carriers reflects the tendency for K and Ta to assume a specific valence state. The difficulty in varying the valence state of the cation greatly retards the ability to make the films semiconducting. Nevertheless, epitaxially grown $\text{KTaO}_3\text{:Ca}$ films grown in 30 mTorr partial pressure of 96% $\text{Ar}/4\% \, \text{H}_2$ atmosphere at $700 \, ^\circ\text{C}$ were semiconducting. The resistivity of $\text{KTaO}_3\text{:Ca}$ film was $10.4 \, \Omega\text{cm}$ at room temperature and showed n-type semiconducting behavior.

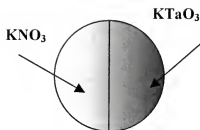


Figure 4-1. Schematic diagram of the segmented $\text{KTaO}_3/\text{KNO}_3$ target

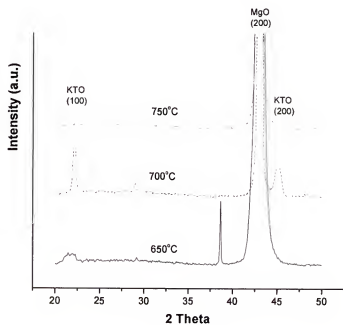


Figure 4-2. X-ray diffraction results of $\text{KTaO}_3:\text{Ca}$ film grown on MgO (100) substrate as a function of deposition temperature.

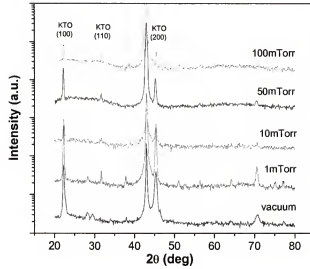


Figure 4-3. X-ray diffraction results of KTaO₃:Ca film grown on MgO (100) substrate as a function of different oxygen pressure at deposition temperature of 700 °C.

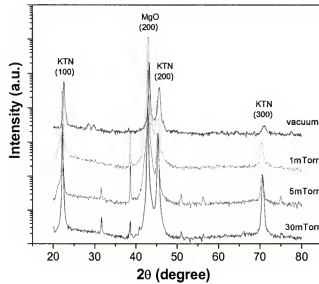


Figure 4-4. X-ray diffraction results of Ca doped KTaO₃ semiconducting film grown on MgO (100) substrate at deposition temperature of 700 °C in reduced pressure of 96% Ar/4% H₂.

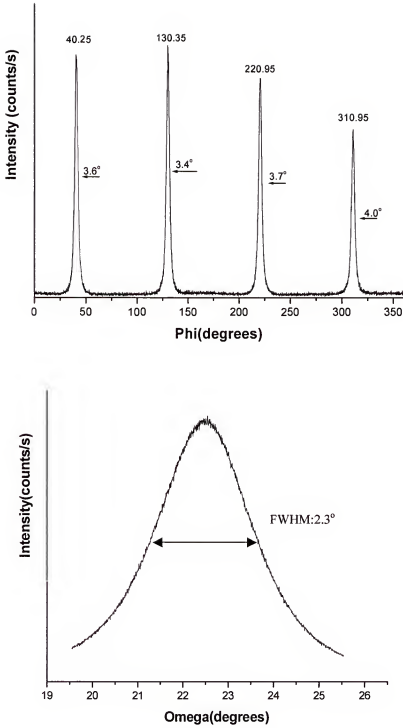


Figure 4-5. X-ray diffraction Φ scan and rocking curve data.



Figure 4-6. FE-SEM images of surface morphology of semiconducting KTO:Ca film on (100) MgO substrate, which was deposited at 700°C for 1hr with 30mTorr of 96%Ar/4% H₂ mixture gas using pulsed laser deposition.

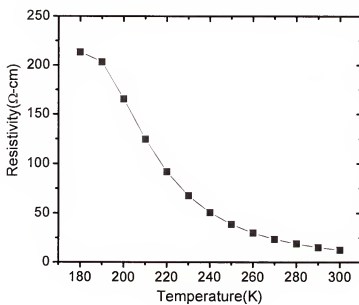


Figure 4-7. Resistivity of Ca doped KTaO₃ thin film as a function of temperature.

CHAPTER 5 DIELECTRIC PROPERTIES OF TI-DOPED K(TA,NB)O₃ THIN FILMS GROWN BY PULSED LASER DEPOSITION

5.1 Introduction

In recent years, perovskite dielectric materials have been considered for application in high density dynamic random access memories, large scale integrated capacitors, phase shifters, band-pass filters, and non-linear optics¹¹¹⁻¹¹⁴. For tunable microwave applications, tunability of the dielectric response under small bias voltage is required¹¹⁵⁻¹¹⁷. For a ferroelectric/paraelectric to be useful in tunable device applications, the material must exhibit a large change in dielectric constant with applied electric field, it must have a low loss tangent with and without applied bias voltage, and the film should have a dielectric constant less than 500 to facilitate insertion into a microwave circuit. Among the perovskite materials considered, Ba_xSr_{1-x}TiO₃¹¹⁸ has received the most attention as a tunable ferroelectric material. However, KTa_{1-x}Nb_xO₃ (KTN) is also an attractive paraelectric / ferroelectric for microwave applications. As with (Ba,Sr)TiO₃, KTa_{1-x}Nb_xO₃ forms a solid solution for $0 \leq x \leq 1.0$ ⁴⁴. KTaO₃ is a cubic paraelectric with a room temperature lattice parameter of 3.9885Å. Doping with Nb yields a ferroelectric KTa_{1-x}Nb_xO₃ solid solution with a Curie temperature, T_c, that increases continuously with increasing x⁴⁶. The end member KNbO₃ undergoes a ferroelectric phase transition at 704 K, changing from cubic (a=4.022Å) to tetragonal (a=b=3.997 Å, c=4.063 Å). Additional structural transitions include an orthorhombic structure (a=4.035 Å, b=3.973 Å, and c=4.035 Å) at 498K and rhombohedral at 265K¹¹⁹. Studies of the dielectric properties of

bulk KTN ceramics and single crystals ^{97,120}, thin films ^{41,110}, and $\text{KTaO}_3/\text{KNbO}_3$ superlattices ^{12,121} indicate dielectric behavior that is very similar to $(\text{Ba,Sr})\text{TiO}_3$, including tunability of the dielectric response with applied electric field.

For tunable dielectrics, a key issue is dielectric loss. While high dielectric tunability has been demonstrated for both $(\text{Ba,Sr})\text{TiO}_3$ and $\text{K}(\text{Ta,Nb})\text{O}_3$ thin films, the accompanying losses are relatively high. A significant fraction of the dielectric loss for these materials is likely associated with donor states due to vacancies on the oxygen sublattice. It is well known that oxygen vacancies in these perovskite materials yield donor states resulting in high loss, or even dc conductive materials, if the defect densities are sufficiently high. One approach to reducing losses previously demonstrated in $(\text{Ba,Sr})\text{TiO}_3$ is acceptor doping ¹²²⁻¹²⁴. For $(\text{Ba,Sr})\text{TiO}_3$ materials, doping with various +2 and +3 valence state cations on the perovskite B-site yields compensating acceptor states. This can lead to a reduction in loss as electrons are trapped on the acceptor sites. Doping studies on $\text{K}(\text{Ta,Nb})\text{O}_3$ have included $\text{K}(\text{Ta,Nb})\text{O}_3$ single crystals doped with Ca or Li to modify the ferroelectric properties by introducing disorder ¹²⁵⁻¹²⁷. However, no studies have addressed reduction of the dielectric losses by means of acceptor doping. In the present study, the effect of Ti doping on the dielectric response of KTN films is investigated. The most stable valence state for Ti is +4, which should provide an acceptor state when substituted on the Nb or Ta site. The ionic radius of Ti^{4+} is 0.605 Å for a coordination number of six. This radius is similar to that for Ta^{5+} (0.64 Å) and Nb^{5+} (0.64 Å), and should yield substitutional doping on the B-site. In this work, the effects of Ti ion substitution on dielectric losses in thin films are investigated. In addition, the influence of Ti doping on dielectric constant and tunability are also reported.

5.2 Experimental Methods

The epitaxial Ti-doped $\text{K}(\text{Ta},\text{Nb})\text{O}_3$ films were grown using pulsed laser deposition. The dielectric properties of the films were measured for materials synthesized over a range of growth conditions. The chosen solid solution was $\text{KTa}_{0.524}\text{Nb}_{0.446}\text{Ti}_{0.03}\text{O}_3$. The bulk ferroelectric transition temperature for a solid solution with an equivalent Ta/Nb ratio ($\text{KTa}_{0.54}\text{Nb}_{0.46}\text{O}_3$) is 70°C . With this compound, the dielectric response both below and above the Curie temperature of the equivalent material with no Ti could be investigated.

$\text{KTa}_{0.524}\text{Nb}_{0.446}\text{Ti}_{0.03}\text{O}_3$ (KTN:Ti) ablation targets were made by solid state synthesis. The starting materials were puratonic grades of K_2CO_3 , Ta_2O_5 , Nb_2O_5 , and TiO_2 . These powders were measured to meet desired composition and then uniformly mixed in methanol base using conventional method. The powders were reacted in air at 900°C for 4 hrs to form KTN:Ti phases. KTN:Ti phases of calcined powders were confirmed by x-ray diffraction method. Then these powders were reground, pressed, and sintered at 1150°C for an additional 20 hrs.

$\text{KTa}_{0.524}\text{Nb}_{0.446}\text{Ti}_{0.03}\text{O}_3$ films were grown on single crystal (001)-oriented MgO substrates. The substrates were ultrasonically cleaned with trichloroethylene, acetone, and methanol, and blown dry with compressed N_2 . In order to compensate for K loss during in-situ film growth, segmented KTN:Ti/ KNO_3 ablation targets were used. Deposition temperatures ranging from 650°C – 750°C were investigated. A KrF (248nm) laser was used as the ablation source. The laser repetition rate was 1Hz with an energy density of $5\text{J}/\text{cm}^2$. Target to substrate distance was fixed at 4cm. Prior to growth, the ablation target was cleaned by pre-ablating 2000 shots. KTN:Ti films were deposited

at various oxygen pressures. Film thickness was measured with a step profilometer. For this study, film thickness was maintained at approximately 250nm. After KTN:Ti film growth, Al/Cr interdigitated electrodes were deposited via RF sputtering. The electrode pattern was defined using lift off photolithography. The length of electrode fingers was 1mm, the finger width was 10 μ m. Distance between the fingers was 10 μ m. The KTN:Ti films were characterized by x-ray diffraction (XRD), atomic force microscopy (AFM), and capacitance measurements. The capacitance measurements included the application of a DC bias voltage in order to probe dielectric tunability. The measurements using HP 4284A LCR meter were performed in air at 1MHz over a temperature range of 20–260°C.

5.3 Results and Discussion

First, $\text{KTa}_{0.524}\text{Nb}_{0.446}\text{Ti}_{0.03}\text{O}_3$ (KTN:Ti) films were grown on (001) oriented MgO single crystals in 100mTorr of oxygen ambient with different growth temperature ranging from 550°C – 750°C. The crystallinity of KTN:Ti films grown on (001) MgO was investigated using x-ray diffraction shown in Figure 5-1, which was using wavelength of 1.5405Å of Cu K α with 40kV and 20mA. KTN:Ti films grown below 650°C were amorphous. The (001) and (002) peaks of KTN:Ti film appeared from growth temperature of 700°C. The high intensity peaks of KTN:Ti films were observed in the KTN:Ti film grown at 750°C with 100mTorr of oxygen ambient.

Epitaxial growth of $\text{KTa}_{0.524}\text{Nb}_{0.446}\text{Ti}_{0.03}\text{O}_3$ (KTN:Ti) thin films was achieved at a growth temperature of 750°C in background pressures ranging from 0.01-150 mTorr. Figure 5- 2 shows the results from θ -2 θ x-ray diffraction (XRD) measurements for KTN:Ti films grown on (001) MgO at different oxygen pressures. The deposition temperature was 750°C for all films considered in Figure 5-2. The XRD results indicate

good crystallinity for all of the KTN:Ti films grown at these conditions. The films are mostly (001) oriented, with only a small KTN (110) peak observed in the diffraction pattern. The Ag peak is from the Ag paint used in mounting the substrates on the heater platen. The intensity of the diffraction peaks are somewhat less for the film grown in vacuum (0.01 mTorr). Note that there is a measurable reduction in c-axis lattice spacing with increasing oxygen pressure during growth. From the θ -2 θ plots, the lattice spacing shifts from 4.0155 Å for films grown in vacuum to 4.0004 Å for films grown in 150 mTorr of oxygen. Larger lattice spacing in oxides often reflects the presence of oxygen vacancies.

The epitaxial relationship of the Ti-doped KTN films on the (001) MgO substrate was investigated using four-circle XRD. Figure 5-3 shows an in-plane ϕ -scan through the KTN:Ti (111) peaks for a film grown at 750°C in 100 mTorr O₂. The full-width half-maximum of the ϕ peak is 1.84°. Despite the lattice mismatch between the KTN film and MgO substrate, the ϕ -scan indicates cube-on-cube in-plane alignment of the KTN:Ti film on the MgO substrate. Also shown in the Figure 5-3 is the rocking curve for the KTN:Ti (002) peak. The full-width half-maximum (FWHM) of the KTN:Ti (002) peak is 0.56°.

Figure 5-4 is the HRTEM images and diffraction patterns at the MgO, the KTN:Ti film and the interface between the MgO substrate and the KTN:Ti film. KTN:Ti film was grown on the (001) MgO substrate at growth pressure of 750°C, and oxygen atmosphere of 100mTorr. The sharp interface between the KTN film and the MgO substrates is observed. And there are no secondary phases at the interface or in the KTN:Ti film.

Figure 5-5 shows the atomic force microscopy (AFM) images of KTN:Ti films grown at different oxygen pressures with deposition temperature of 750°C. The grain

size for all oxygen pressures is on the order of 400-500 nm. It should be noted that micro-cracks were observed due to stress in KTN:Ti films on MgO more than 3000Å of thickness. These films were easily peeled off due to residual stress in film after film growth.

The dielectric response of the films was measured using the interdigitated electrodes. Figure 5-6 shows the measured capacitance for KTN:Ti films on MgO single crystals grown in various oxygen pressures at a growth temperature of 750°C. Also, film thicknesses of all grown films were fixed around 250nm. Therefore, the measured capacitance values could be possible to compare the KTN:Ti films grown at different oxygen pressures. Capacitance measurements were made for an applied bias voltage ranging from 0 to 40 volts and were performed at 30°C with a measurement frequency of 1MHz. With the exception of the film grown at 10^{-5} Torr, the capacitance for films grown at oxygen pressures ranging from 50-150 mTorr was constant. A reduction in dielectric constant with acceptor doping has also been observed in (Ba,Sr)TiO₃ thin films. Note that the high capacitance for KTN:Ti films grown at 10^{-5} Torr reflects the high loss tangent of this film due to a high density of oxygen vacancies. Also note that the KTN:Ti films grown at $P(O_2) \geq 50$ mTorr show or moderate voltage tunability as will be discussed later.

The capacitance of the titanium-doped films was then measured at various temperatures. The temperature dependence of the dielectric properties for films grown at 750°C in various oxygen pressures was also measured as shown in Figure 5-7. Measurements were made at temperatures ranging from 50–240°C at a fixed de bias of 10V and a measurement frequency of 1MHz. For films grown at $P(O_2) \leq 50$ mTorr, the measured capacitance significantly increases as the measurement temperature increases.

Again, this reflects the activation of a high density of donor defects in films grown under these conditions. These defects were electrically active at higher temperatures. This is also reflected in the dielectric loss measurements discussed later. However, for films grown at oxygen pressures equal to or greater than 100mTorr, the capacitance slightly decreases as temperature increases. This is the expected behavior for temperature biasing a ferroelectric material deeper into the paraelectric regime above T_c .

The motivation for investigating titanium doping is to potentially reduce the losses due to defect donor states. The dielectric loss behavior for KTN:Ti films grown at various oxygen pressures is shown in Figure 5-8. Dielectric loss measurements were carried out at 30°C, at a frequency of 1MHz under an electric field in the range of 0–40kV/cm. For KTN:Ti films grown in vacuum, the dielectric loss is high and is quite sensitive to applied bias voltage. Again, this reflects a high density of oxygen vacancies for films grown in vacuum. However, the loss tangent for KTN:Ti films grown with oxygen pressure greater than 50mTorr is quite low. From the dielectric loss data, the loss tangent for these films is estimated to be less than 0.02. This is 50% lower than that found for Ti-free KTN films grown under the same conditions.

The tunability in dielectric response was measured for the films grown under all conditions, with particular interest in those films grown at oxygen pressures greater than or equal to 50mTorr, as these exhibit reasonably low losses. Figure 5-9 shows the electric field dependent of capacitance and calculated tunability of the dielectric response for a KTN:Ti film grown at $P(O_2)=150$ mTorr. Measurements were made at a room temperature and a frequency of 1MHz. The films exhibit a tunability of 14% for an applied electric field of 40kV/cm. This is somewhat smaller than that observed for KTN

films that do not contain Ti, where the tunability can exceed 40%. A reduction in tunability with acceptor doping has also been observed in (Ba,Sr)TiO₃ thin films. Figure 5-10 is tunability $(= (C(E_0) - C(E_{\max})) / C(E_0) \times 100)$ and loss tangent of KTN:Ti films grown on (001) MgO at different growth pressures with deposition temperature of 750°C. Capacitance was measured at 20°C, 1MHz. Tunability of KTN:Ti films decreases as P(O₂) increased. Films grown P(O₂) ≥ 100mTorr exhibit a tunability on the order of 10%. However, loss tangent of films grown at P(O₂) ≥ 100mTorr are most relevant as these have low losses.

Figure 5-11 shows the Figure of Merit, which is also known as K-factor for indication of the performance for tunable microwave devices. FOM is calculated by means of dividing tunability by maximum loss tangent. The highest FOM is observed in KTN:Ti film grown at 750°C and 100mTorr oxygen atmosphere because FOM is dominated by lower loss tangent.

Figure 5-12 shows capacitance and calculated tunability of KTN:Ti films as a function of measurement temperature. KTN:Ti film was grown on (001) MgO at deposition temperature of 750°C, and oxygen atmosphere of 150mTorr. Capacitance decreases as a measurement temperature increases. Also, tunability decreases as a measurement temperature increases. This consists with paraelectric behavior in the deeper region from curie temperature. The highest tunability is observed at room temperature. From this results, we can assume curie temperature, T_c, of KTN:Ti film is lower than room temperature.

Loss tangents of undoped KTN and KTN:Ti are compared in Figure 5-13. Both films were prepared in same condition. Loss tangent of undoped KTN increased as a

measurement temperature increased. However, loss tangent of Ti doped KTN had no significant change along with the measurement temperatures. This result proves Ti ions, which were doped as acceptor ions, effectively trap electron charges even at high temperature.

5.4 Conclusion

The dielectric properties of Ti doped KTN films were studied. The growth conditions of KTN:Ti films are a major factor in determining dielectric properties. KTN:Ti film grown without oxygen showed high dielectric constant but with high loss tangent due to oxygen vacancies in KTN:Ti film. Tunability of KTN:Ti films grown at above oxygen pressures of 100mTorr was approximately 10–14% with loss tangent around 0.02. Tunability and loss are reduced by Ti doping.

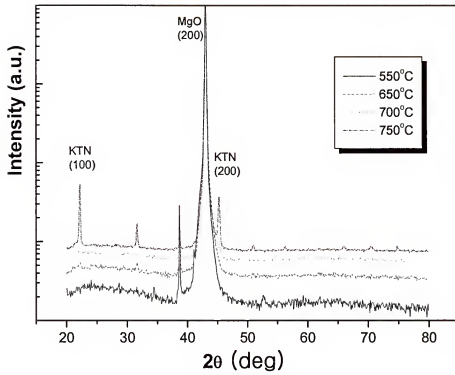


Figure 5-1. XRD results of KTN:Ti films grown at different growth temperature with 100mTorr of oxygen atmosphere and 1Hz of frequencies.

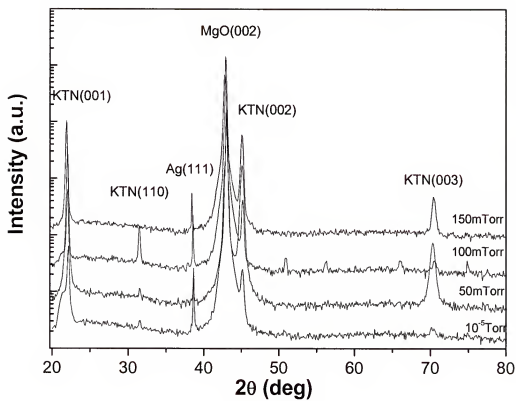


Figure 5-2. XRD results of KTN:Ti films grown at different oxygen pressure with deposition temperature 750°C.

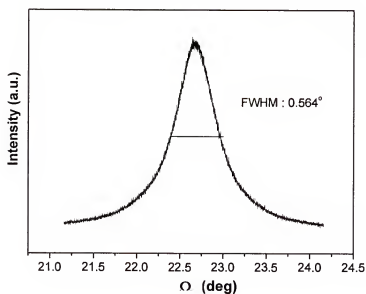
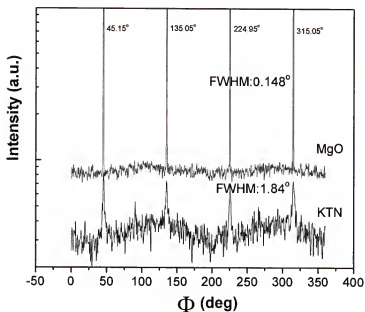


Figure 5-3. Four circle XRD results of KTN:Ti films grown at 100mTorr oxygen pressure with deposition temperature 750°C . (a) phi scan for the (111) reflection of KTN:Ti and MgO, and (b) the rocking curve of (200) KTN:Ti film: FWHM is 0.564° .

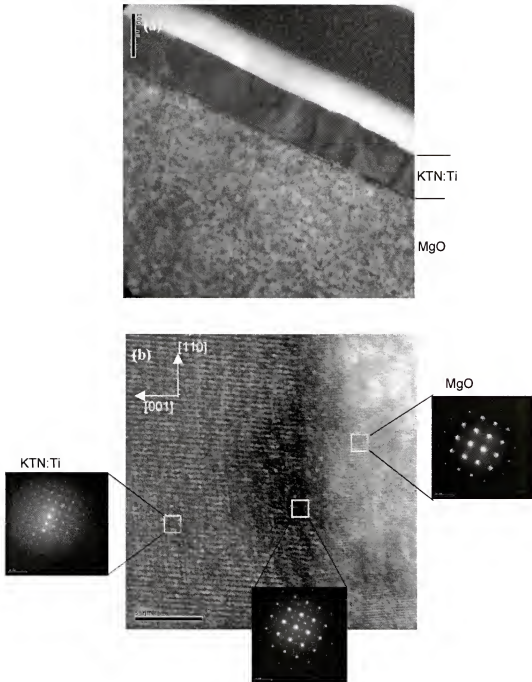


Figure 5-4. TEM images of KTN:Ti films grown on MgO single crystals at 750°C of growth pressure, and 100mTorr of oxygen atmosphere

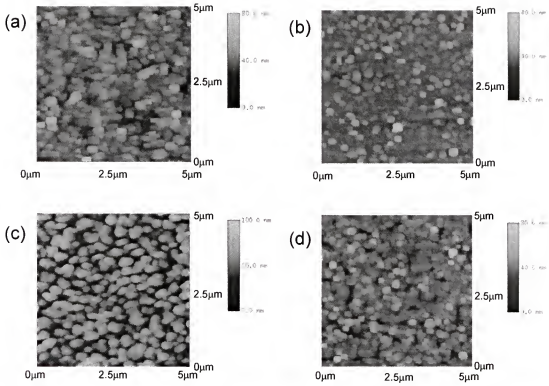


Figure 5-5. AFM images of KTN:Ti films grown at different oxygen pressure with deposition temperature 750°C : (a) vacuum, (b) 50mTorr (c) 100mTorr and (d) 150mTorr

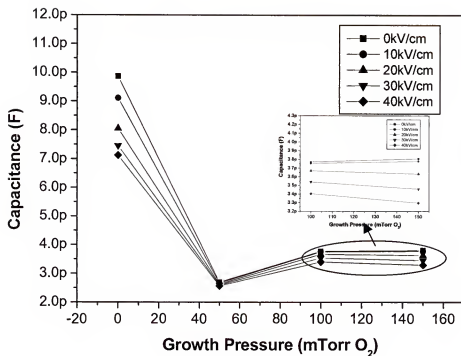


Figure 5-6. Results of capacitance of KTN:Ti films on MgO single crystals as a function of oxygen growth pressure under 0, 10, 20, 35, and 40V dc bias voltage measured at 30°C, and frequency of 1MHz

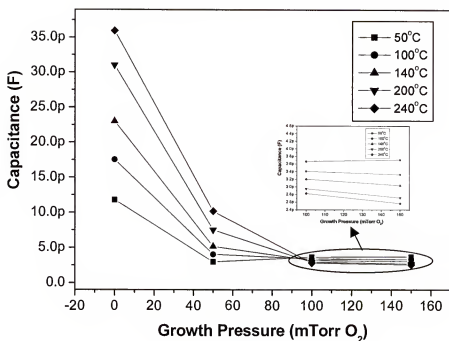


Figure 5-7. Oxygen pressure dependence of capacitance for KTN:Ti films on MgO single crystals under temperature in the range of 50 – 240°C at dc bias of 10V, and frequency of 1MHz

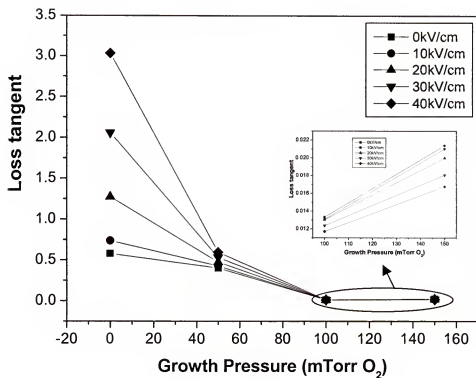


Figure 5-8. Oxygen pressure dependence of loss tangent for KTN:Ti film on MgO single crystal under dc bias in the range of 0 – 40kV/cm at temperature of 30°C, and frequency of 1MHz

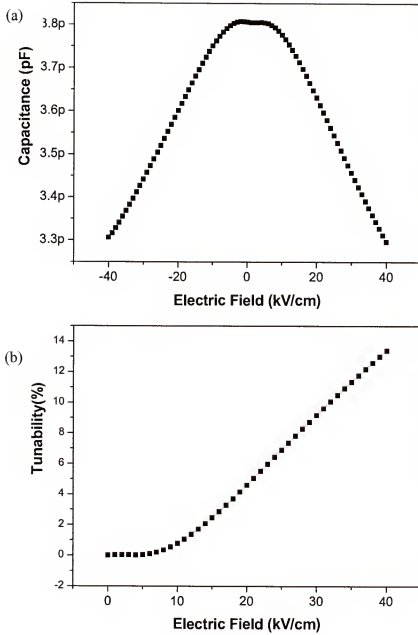


Figure 5-9. DC bias voltage dependence of (a) capacitance and (b) tunability for KTN:Ti film on MgO at room temperature at 1MHz frequency. KTN:Ti film was grown at 150mTorr of oxygen with deposition temperature 750°C

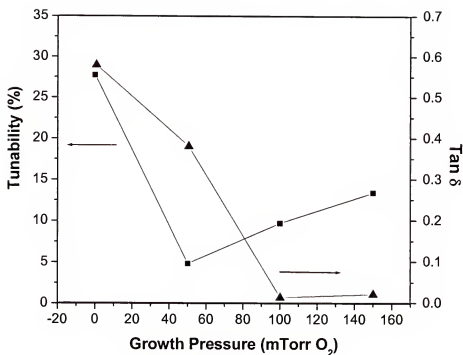


Figure 5-10. Tunability ($= (C(E_0) - C(E_{\max})) / C(E_0) \times 100$) and loss tangent of KTN:Ti film grown on (001) MgO at different growth pressure with deposition temperature 750°C

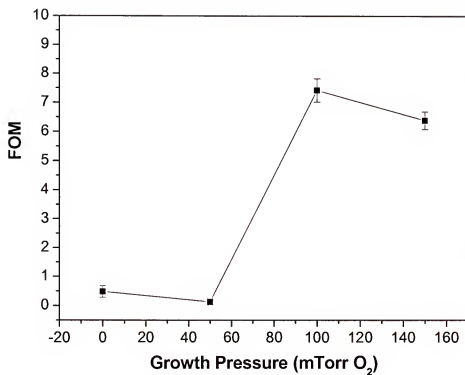


Figure 5-11. Figure of merit (FOM=tunability/loss tangent) of KTN:Ti film grown on (001) MgO at different growth pressure with deposition temperature 750°C

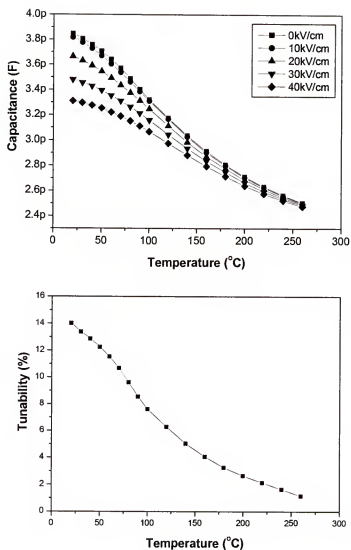


Figure 5-12. Capacitance and tunability of KTN:Ti film as a function of measurement temperature. KTN:Ti film was grown on (001) MgO at deposition temperature 750°C, and 150mTorr of oxygen atmosphere

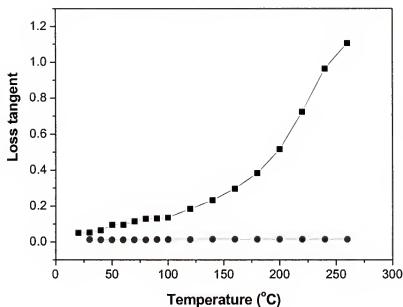


Figure 5-13. Comparison of loss tangent of undoped KTN and KTN:Ti film as a function of measurement temperature. Both films were grown on (001) MgO at 750°C of deposition temperature, and 100mTorr of oxygen atmosphere for 1hr. (■: loss tangent of KTN, ●: loss tangent of KTN:Ti films)

CHAPTER 6
LOW DIELECTRIC LOSSES IN ANNEALED TI-DOPED K(TA,NB)O₃ THIN FILMS
GROWN BY PULSED LASER DEPOSITION

6.1 Introduction

In previous chapter 5, we studied dielectric properties of as-deposited KTN:Ti films on (001) MgO substrates with various conditions such as changing growth temperature, growth pressure of KTN:Ti films.

In this chapter, we will focus on dielectric properties of KTN:Ti films on (001) MgO substrates by annealing the films at various temperatures for 2hrs in oxygen ambient. Growth conditions were optimized to 750°C of growth temperature, 100mTorr of oxygen pressure, and 250nm of film thickness.

6.2 Experimental Methods

First, KTN:Ti films were grown on single crystal (001)-oriented MgO substrates. The substrates were ultrasonically cleaned with trichloroethylene, acetone, and methanol, and blown dry with compressed N₂. In order to compensate for K loss during in situ film growth, segmented KTN:Ti/KNO₃ ablation targets were used. A KrF (248nm) laser was used as the ablation source. The laser repetition rate was 1Hz with an energy density of 5J/cm². Target to substrate distance was fixed at 4cm. KTN:Ti films were deposited at 750°C, and 100mTorr of oxygen pressure. Film thickness was measured with a step profilometer. For this study, film thickness was maintained at approximately 250nm. After KTN:Ti film growth, the films were placed inside tube furnace to be annealed in oxygen atmosphere. Oxygen ambient was created by flowing oxygen of 50sccm from one

side of quartz tube through thermal heating zone. Ramping speed of temperature was 5°C/min to desired annealing temperature, and then temperature was held to 2 hrs. Cooling down was conducted as same speed as ramping up. For dielectric measurements, Al/Cr interdigitated electrodes were then deposited via RF sputtering. The electrode pattern was defined using lift off photolithography. The annealed KTN:Ti films were characterized by x-ray diffraction (XRD), atomic force microscopy (AFM), and capacitance measurements.

6.3 Results and Discussion

Epitaxial $\text{KTa}_{0.524}\text{Nb}_{0.446}\text{Ti}_{0.03}\text{O}_3$ (KTN) thin films were grown at 750°C in 100 mTorr of oxygen pressure. Figure 6-1 shows the results from θ -2 θ x-ray diffraction (XRD) measurements using Cu $K\alpha$ radiation at 40kV and 20mA for KTN:Ti films grown on (001) MgO and annealed at different temperatures ranging from 800 – 1000°C in oxygen ambient. The deposition temperature was 750°C for all films considered in Figure 6-1. The XRD results indicate good crystallinity for all of these annealed KTN:Ti films. The films are mostly (001) oriented, with only a small KTN (110) peak observed in the diffraction pattern up to 900°C of annealing temperature. The Ag peak is from the Ag paint used in mounting the substrates on the heater platen. However, secondary phases of KTN:Ti film were exhibited in XRD result of KTN:Ti film annealed at 1000°C for 2hrs. These secondary phases were resulted from decomposition of potassium during annealing at high temperature.

Figure 6-2 shows lattice constant of KTN:Ti films as a function of annealing temperature. As annealing temperature increased, lattice constants of KTN:Ti film

increased to reduce strain caused by lattice mismatch between MgO ($a=4.210\text{\AA}$) and KTN:Ti.

The epitaxial relationship of the annealed Ti-doped KTN films on the (001) MgO substrate was investigated using four-circle XRD. Figure 6-3 shows an in-plane ϕ -scan through the KTN:Ti (111) reflection for a film grown at 750°C in 100 mTorr O_2 and then annealed at 900°C for 2hrs. The full-width half-maximum of the ϕ peak is 2.689° . Despite the lattice mismatch between the KTN film and MgO substrate, the ϕ -scan indicates cube-on-cube in-plane alignment of the KTN:Ti film on the MgO substrate. Also shown in Figure 6-3 is the rocking curve for the KTN:Ti (200) peak. The full-width half-maximum (FWHM) of the KTN:Ti (200) peak is 0.566° . The FWHM of annealed KTN:Ti film is similar to that of unannealed KTN:Ti. The annealing of KTN:Ti film at 900°C does not change in crystal qualities compared to the unannealed KTN:Ti film.

Figure 6-4 shows AFM images of as-deposited and annealed KTN:Ti films. Surface morphologies of annealed KTN:Ti film started to change with a 900°C anneal. Grain size of KTN:Ti film increased as annealing temperature increased. After annealing at 1000°C , large grains were observed. Grain size increased from 250nm to 1 μm compared to as-deposited and KTN:Ti film annealed at 1000°C . Also, small second phases were observed on the surface and grain boundaries of KTN:Ti film annealed at 1000°C for 2 hrs. The appearance of these second phases correlates with unknown peaks in XRD (Figure 6-1.).

The dielectric response of the films was measured using the interdigitated electrodes. The temperature-dependent tunability of titanium-doped films annealed at various temperatures is shown in Figure 6-5. The KTN:Ti films were annealed at 800 and

900°C for 2hrs. Tunability of annealed KTN:Ti film is clearly lower than as-deposited KTN:Ti films on MgO. Measurements were made at temperatures ranging from 20 – 260°C and a measurement frequency of 1MHz. For films at higher temperatures, the tunability clearly decreases with increasing annealing temperature. The decrease in tunability with increasing measurement temperature is consistent with temperature biasing a ferroelectric material deeper into the paraelectric regime above T_c .

The primary motivation for investigating titanium doping is to reduce the losses due to defect donor states. The dielectric loss behavior for KTN:Ti films annealed at various temperatures is shown in Figure 6-6. Loss tangent measurements were carried out over a temperature range of 20-260°C, at a frequency of 1MHz under a dc bias of 0V with oscillation voltage of 0.1V. The films were annealed for 2 hrs. For KTN:Ti films annealed in oxygen, the loss tangent is clearly reduced with annealing in oxygen ambient. This reflects both a reduction in oxygen vacancies and an activation of the Ti as an acceptor impurity. From the dielectric response, the loss tangent for films annealed at 900°C is as low as 0.002. This is significantly lower than that found for unannealed Ti-KTN films grown under the same conditions. The films show little change in loss with increasing temperature, again indicative of a reduction in donor states due to defects.

Figure 6-7 shows the capacitance and Figure of merit for a KTN:Ti film on MgO annealed at 900°C for 2hrs as a function of electric field. The KTN:Ti film on MgO was grown at 750°C with 100mTorr of oxygen ambient. The observed tunability is lower than that observed for films without Ti, although the dielectric loss is lower. Capacitance measurements were made for an applied bias voltage ranging from -40 to 40 volts and were performed at 20°C with a measurement frequency of 1MHz. The titanium doping

yields a lower dielectric constant relative to the undoped material. A reduction in dielectric constant with acceptor doping has also been observed in (Ba,Sr)TiO₃ thin films.

Figure 6-8 shows the capacitance of KTN:Ti film on (001) MgO substrate, which was annealed at 900°C for 2hrs. The capacitance measurement was conducted in a temperature ranging 20 – 260°C under different electric fields. The measured capacitance of KTN:Ti film decreased as temperature increased. This is consistent with paraelectric behavior far removed from the ferro – and paraelectric transition temperature, T_c .

Figure 6-9 shows the dielectric loss of KTN:Ti film annealed at 900°C for 2hrs in oxygen ambient as a function of different measurement temperatures under different electric field. Difference in loss $((\text{Loss}(E_0) - \text{Loss}(E_{\max})) / \text{Loss}(E_0) \times 100)$ at 20°C was 13%. This difference decreased as temperature increased. The dielectric loss was changed from 0.0027 at 20°C to 0.0001 at 240°C. The dielectric loss of KTN:Ti film significantly decreased as measurement temperature increased.

FOM of as-deposited KTN:Ti film and annealed KTN:Ti film was shown in Figure 6-10. KTN:Ti film was annealed at 900°C with oxygen ambient. Tunability of as-deposited film was higher than that of annealed KTN:Ti film (Figure 6-5.). However, dielectric loss of annealed KTN:Ti film was lower than that of as-deposited KTN:Ti film. Therefore, FOM of annealed KTN:Ti film was better than that of as-deposited KTN:Ti film in overall range of measurement temperatures.

6.4 Conclusion

The dielectric properties of annealed Ti doped KTN films were studied. The annealing treatment of KTN:Ti films significantly influences the dielectric properties. As-deposited KTN:Ti films show relatively high dielectric loss due to oxygen vacancies. By annealing in oxygen, the dielectric loss and tunability are reduced.

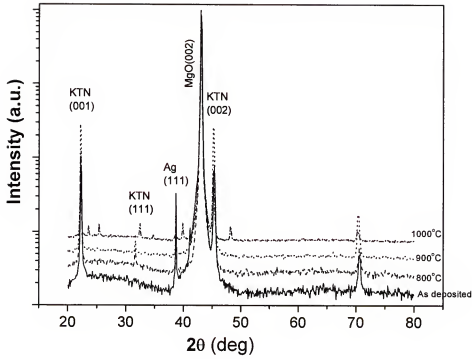


Figure 6-1. XRD results of KTN:Ti films annealed at different temperatures. KTN:Ti films were grown at 750°C of deposition temperature, and 100mTorr of oxygen pressure

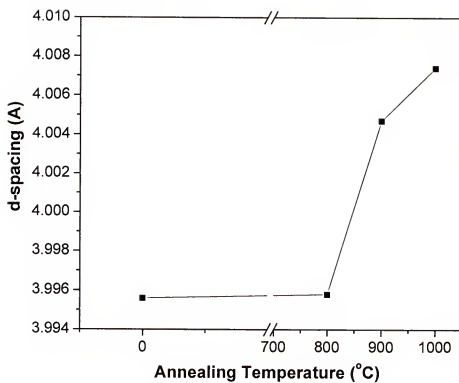


Figure 6-2. Lattice spacing of KTN:Ti films annealed at different temperatures

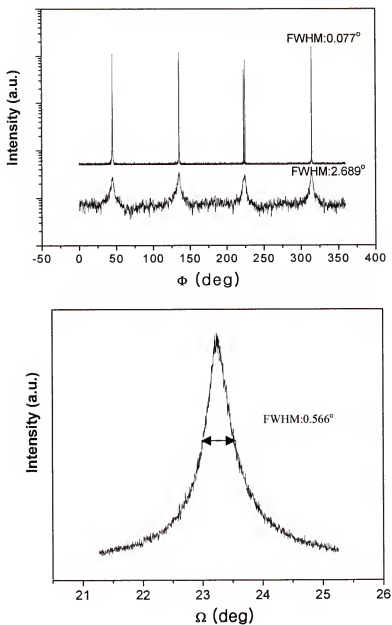


Figure 6-3. Four circle XRD results of KTN:Ti film annealed at 900°C for 2hrs. KTN:Ti film was grown at 100mTorr oxygen pressure with deposition temperature 750°C. (a) ϕ scan for the (110) reflection of KTN:Ti and MgO, and (b) the rocking curve of (200) KTN:Ti film: FWHM is 0.566°

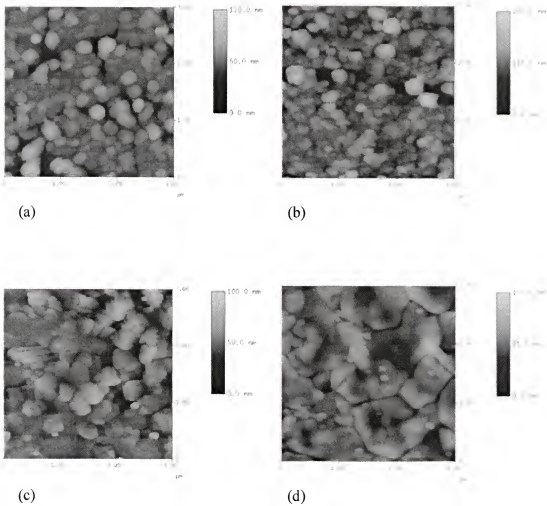


Figure 6-4. AFM images of KTN:Ti films annealed at different temperature with oxygen ambient for 2hrs. Growth condition of KTN:Ti films were 750°C deposition temperature, 100mTorr of oxygen pressure and 1Hz of frequencies : (a) without annealing, (b) annealed at 800°C, (c) annealed at 900°C, and (d) annealed at 1000°C

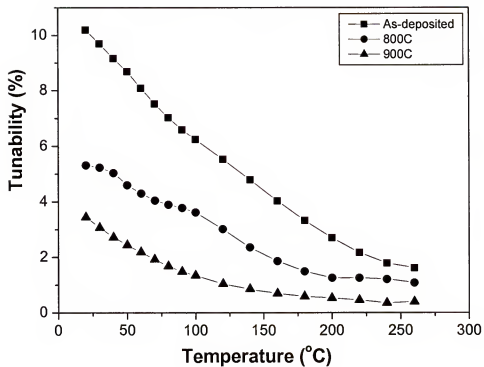


Figure 6-5. Results of tunabilities of as-deposited and annealed KTN:Ti films as a function of measurement temperature. Tunability $((C(E_0) - C(E_{max})) / C(E_0) \times 100)$ was measured at 0 - 40kV/cm of electric field range, 1MHz frequency

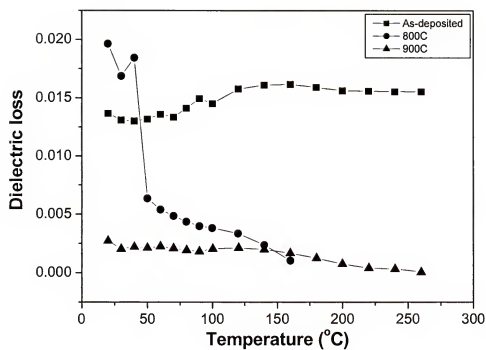


Figure 6-6. Results of dielectric loss of as-deposited and annealed KTN:Ti films as a function of measurement temperature

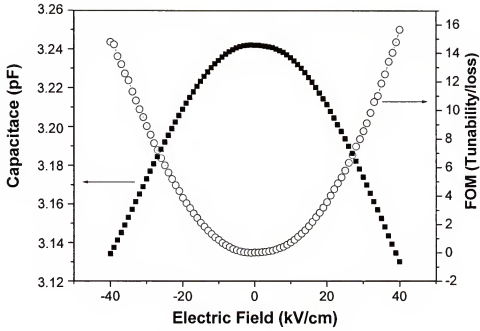


Figure 6-7. Results of capacitance and FOM for KTN:Ti film on MgO annealed at 900°C for 2hrs at room temperature as a function of electric field

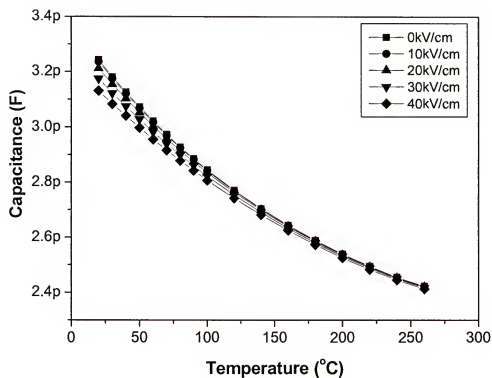


Figure 6-8. Temperature dependence of capacitance for KTN:Ti film on MgO at temperature of 20°C at 1MHz frequency under different electric field ranging 0 – 40kV/cm. KTN:Ti film was grown at 100mTorr of oxygen with deposition temperature 750°C and then annealed at 900°C for 2hrs

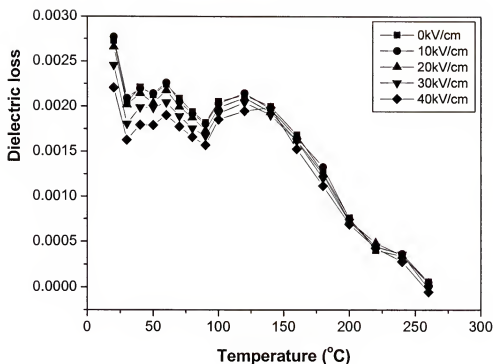


Figure 6-9. Temperature dependence of dielectric loss for KTN:Ti film on MgO at temperature of 20°C at 1MHz frequency under different electric field ranging 0 – 40kV/cm. KTN:Ti film was grown at 100mTorr of oxygen with deposition temperature 750°C and then annealed at 900°C for 2hrs

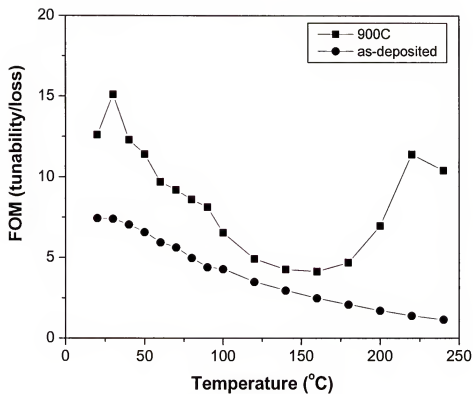


Figure 6-10. Comparison of FOM of as – deposited and 900°C annealed KTN:Ti films on MgO with different measurement temperature at 1MHz frequency

CHAPTER 7

THICKNESS DEPENDENT TUNABILITY FOR TI-DOPED K(Ta,Nb)O₃ FILM BY PLD

7.1 Introduction

Ferroelectric materials have been widely investigated for its useful properties, which could be applied for optical wave-guide, ferroelectric random access memory, and tunable microwave devices¹¹¹⁻¹¹⁴. Among the materials of interest, K(Ta,Nb)O₃ has intriguing structural and electric properties for many applications. KTaO₃ is a paraelectric material with a cubic structure ($a=3.9885$) at all temperatures. KNbO₃ is a ferroelectric with a curie temperature of 704K and three structural phase transition temperatures¹¹⁹. KTaO₃ and KNbO₃ form a solid solution, namely KTa_{1-x}Nb_xO₃. The dielectric and structural properties of K(Ta,Nb)O₃ have motivated activity to investigate the properties of K(Ta,Nb)O₃ films for tunable microwave application such as phase filters, frequency-agile filters, voltage-controlled oscillators, and antennas^{128,129}. For tunable microwave applications, a high dielectric constant, relatively low dielectric loss, large electric field nonlinearity, and high figure of merit are required. As the thickness of dielectric thin film materials is decreased, dielectric properties often modified. There are several factors that contribute to deviations from bulk-like properties, including; growth conditions, crystal quality, strain at the interface, and dead layer near the interface^{20,130-131}.

There have been numerous studies on size effects that modify the effective dielectric constant in ferroelectric thin films^{132,133}. According to the studies of Zhou and Newns¹³⁴, and Natori et al¹³⁵, the surfaces of high dielectric films have a low

permittivity layer due to an intrinsic dead layer¹³⁰. Thickness of this intrinsic dead layer is established to be on the order of 1nm. However, changes in dielectric properties are observed for film thicknesses much larger than this. In the previous works, we investigated the dielectric properties of acceptor ion (Ti) doped KTN thin films¹³⁶. In this study, the thickness dependent dielectric properties, namely the tunability, of KTN:Ti thin films is reported.

7.2 Experimental Methods

The epitaxial Ti-doped K(Ta,Nb)O₃ films were grown using pulsed laser deposition. The chosen solid solution was KTa_{0.524}Nb_{0.446}Ti_{0.03}O₃. The bulk ferroelectric transition temperature for a solid solution with an equivalent Ta/Nb ratio (KTa_{0.54}Nb_{0.46}O₃) is 70°C. KTa_{0.524}Nb_{0.446}Ti_{0.03}O₃ (KTN:Ti) ablation targets were synthesized with raw materials of K₂CO₃, Ta₂O₅, Nb₂O₅, and TiO₂ by solid state reaction. The powders were calcined to remove carbonate and form KTN:Ti in air at 900°C for 4 hrs. And then the reacted powders were reground, pressed, and sintered at 1150°C for an additional 20 hrs.

KTa_{0.524}Nb_{0.446}Ti_{0.03}O₃ films were grown on single crystal (001)-oriented MgO substrates. Prior to film growth, the one-side polished MgO substrates were ultrasonically cleaned with trichloroethylene, acetone, and methanol, and blown dry with compressed N₂. In order to compensate for K loss during in situ film growth, segmented KTN:Ti/KNO₃ ablation targets were used. A KrF (248nm) laser was used as the ablation source. The laser repetition rate was 1Hz with an energy density of 5J/cm². Target to substrate distance was fixed at 4cm. Prior to growth, the ablation target was cleaned by pre-ablating 2000 shots. KTN:Ti films were deposited at 750°C with 100mTorr of

oxygen pressure. Film thickness was measured with a step profilometer. For this study, film thickness was chosen to be 90, 180, 250nm. For dielectric measurements, Al/Cr interdigitated electrodes were then deposited via RF sputtering. The electrode pattern was defined using lift off photolithography. The length of electrode fingers was 1mm, the finger width was 10 μ m. Distance between the fingers was 10 μ m. The KTN:Ti films were characterized by x-ray diffraction (XRD), atomic force microscopy (AFM), and capacitance measurements. The capacitance measurements included the application of a DC bias voltage in order to probe dielectric tunability. The measurements were performed in air at 1MHz over a temperature range of 20 – 260°C using an Agilent 4284A precision LCR meter.

7.3 Results and Discussion

Films grown under the prescribed conditions were epitaxial with respect to the (100) MgO substrate. Figure 7-1 shows X-ray diffraction results of KTN:Ti film on MgO. The (00 l) peaks for KTN:Ti film are clearly observed in all of XRD results. The intensity of (001) peak of KTN:Ti film on MgO increased as film thickness increased. Four-circle x-ray diffraction Φ -scan data shows that the KTN:Ti films were in-plane aligned on (001) MgO. The full width at half maximum (FWHM) of the omega scan peaks for the (002) KTN:Ti reflection was 0.56°.

Figure 7-2 shows AFM images of the KTN:Ti films on MgO substrates. AFM images were obtained with a 3 x 3 μ m scan area of surface using contact mode. The root-mean-square (rms) roughness of KTN:Ti films ranged from 9.9 to 12.1 nm. Grain sizes were on the order of 100-200 nm.

The dielectric properties were measured at 1MHz frequency. A dc bias of $\pm 40\text{kV/cm}$ electric field was applied to probe tunability. The measurement temperature ranged for $25 - 260^\circ\text{C}$. Figure 7-3 shows interdigitated electrode capacitance as a function of KTN:Ti film thickness. As expected, the capacitance of the KTN:Ti film increased as thickness of the film increased. At elevated temperatures, capacitance values of KTN:Ti film were lower than that measured at room temperature, irrespective of the thickness of KTN:Ti films. This is consistent with a paraelectric material that is temperature tuned to just above the Curie temperature.

Figure 7-4 shows capacitance data of KTN:Ti films on MgO (100) as a function of applied electric field up to $\pm 40\text{kV/cm}$ with different film thicknesses. The capacitance tuning with applying electric field was small for the KTN:Ti film with thickness of 90nm . This capacitance tuning increased as film thickness increased. Also, capacitance values increased as film thicknesses increased.

The tunability of the KTN:Ti films are shown in Figure 7-5. The tunability is calculated using following equation.

$$\text{Tunability}(\%) = \frac{C(0) - C(E_{\max})}{C(0)} \times 100$$

where $C(0)$ is the zero-field capacitance, $C(E_{\max})$ is the capacitance under maximum bias. Tunability increased as KTN:Ti film thickness increased. Tunabilities of the KTN:Ti thin film structures were 3.8, 8.2, and 10.3% for film thicknesses of 90nm , 180nm , and 250nm , respectively.

The interdigitated electrode capacitance measurements obvious include the effects of the film, substrate, and air. A simple approximation is to assume a parallel capacitor model as shown in the Figure 7-6. If one changes the film thickness, the only

parameter in this model that changes is C_2 . If one assumes that the capacitance from the film is proportional to film thickness, one predicts a linear relationship between capacitance and film thickness. This is what is observed in Figure 7-3. From this, one can extract the parasitic capacitance from the air and substrate for the particular interdigitated electrode configuration. For the devices considered, this yields a parasitic capacitance of 1.18pF. If this becomes possible to compare the change in capacitance with applied electric field to the capacitance due to the field, assuming that the contribution to tunability from the substrate is minimal, one can more effectively compare tunability for films with different thickness through the parameter shown in Figure 7-7.

$$Tunability = \frac{C_f(0) - C_f(E_{max})}{C_f(0)}$$

Using this, we get the following (called intrinsic tunability)

$$t=90nm \Rightarrow tunability= 7.6\%$$

$$180nm \Rightarrow tunability= 11.6\%$$

$$250nm \Rightarrow tunability= 10.9\%$$

where C_f is the capacitance of thin film.

Note that the intrinsic tunability for the two thicker films is essentially the same, which to some degree, justifies the approximations used in this analysis. Second, the tunability for the 90nm thick film is notably smaller than for the thicker films. This would suggest that the electrostatic displacements that yield dc tunability of the dielectric constant experience some degree of pinning in the thinner film.

The Figure of Merit (FOM) was used to evaluate the material properties for tunable microwave devices.

$$FOM = \frac{C(0) - C(E_{\max})}{C(0)} \times \frac{1}{\tan(\delta)_{\max}}$$

Figure 7-8 shows the FOM of KTN:Ti films on (001) MgO as a function of applied electric field upto 40kV/cm. The FOM values at 40kV/cm are 4.2, 8.4, and 8.5 for 90nm, 180nm, 250nm thickness of KTN:Ti film, respectively. There is no change in FOM for KTN:Ti film thickness above 180nm.

Figure 7-9 shows the capacitance results of the KTN:Ti film structures as a function of measurement temperature. Capacitances of each of samples decrease as measurement temperature is increased. This is consistent of paraelectric behavior in a deeper region from the transition temperature (T_c). Also, the capacitance was higher in the thicker film. Mostly, capacitances are a function of thickness. Also, the transition temperature of these KTN:Ti films would be lower than room temperature.

Figure 7-10 shows the loss tangent δ results as a function of measurement temperature. The dielectric loss in 90nm thickness of KTN:Ti film was below 0.0095 over the measurement temperature range up to 260°C. However, dielectric losses increased as film thickness increased. In 180nm and 250nm thickness of KTN:Ti films, dielectric losses increased as the measurement temperature increased. This behavior resulted from thermally activated electrons by oxygen vacancies. The number of defects (or density of defects) such as oxygen vacancies increased as film thickness increased. Therefore, dielectric loss was higher in thicker KTN:Ti film. However, overall dielectric losses were below 0.017 over the temperature ranging up to 260°C.

Figure 7-11 shows the tunability of KTN:Ti film on MgO as a function of measurement temperature. Tunabilities decreased as temperature increased. In thicker

film, tunability variance was larger than in thinner film from room temperature up to 260°C.

Figure 7-12 shows the FOM of KTN:Ti film on MgO as a function of capacitance measurement temperature. The FOM also decreased as temperature increased. In higher temperature range, the tunabilities of KTN:Ti films with different film thickness were closed each other than in low temperature range. Also, there are no big difference in FOM value of KTN:Ti films of 180nm, and 250nm thickness in low temperature region.

7.4 Summary

In this study, KTN:Ti films with different thicknesses were grown on (001) MgO substrates in a condition of 750 °C of growth temperature, and 100 mTorr of oxygen ambient. The dielectric properties of these films were measured using Agilent HP 4284A precision LCR meter at $\pm 40\text{kV/cm}$, 1MHz frequency under different measurement temperatures. Thicker KTN:Ti film shows the higher capacitance than thinner KTN:Ti film. Also, tunability of KTN:Ti film increased as film thicknesses increased. Although dielectric loss is higher in thicker film, FOM in thicker film is higher than in thinner film.

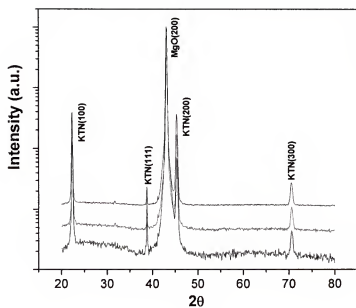


Figure 7-1. XRD results of KTN:Ti films on (100) MgO substrates grown at 750 °C, 100 mTorr of oxygen ambient with different film thicknesses

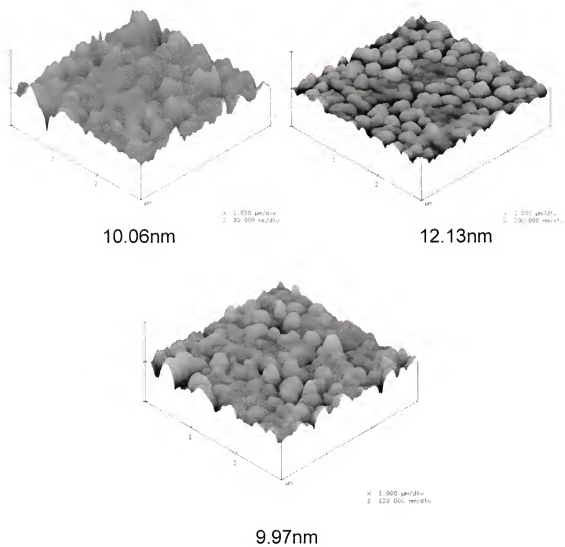


Figure 7-2. AFM images for surface morphologies of KTN:Ti films on (100) MgO substrates : (a) 90 nm, (b) 180 nm, and (c) 250 nm of KTN:Ti film thickness. AFM images taken in area of $3 \times 3 \mu\text{m}$ using contact mode

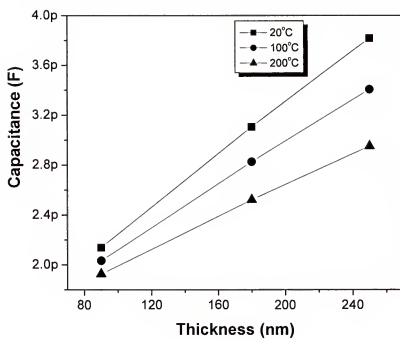


Figure 7-3. Capacitance as a function of the thickness of KTN:Ti film under different measurement temperatures

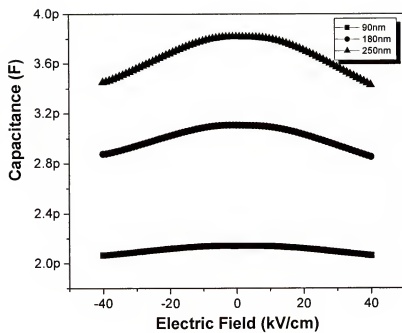


Figure 7-4. Capacitance data of KTN:Ti films on MgO (100) as a function of applying electric field up to ± 40 kV/cm with different film thicknesses

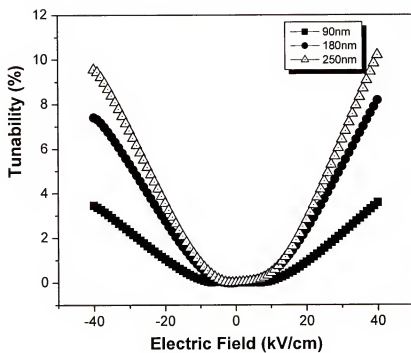
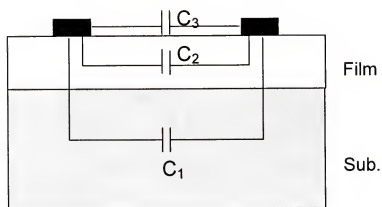


Figure 7-5. Tunabilities of KTN:Ti films as a function of electric field with different film thicknesses



$$C_{\text{tot}} = C_1 + C_2 + C_3$$

Figure 7-6. Simplified IDC structure of KTN:Ti films on MgO substrate

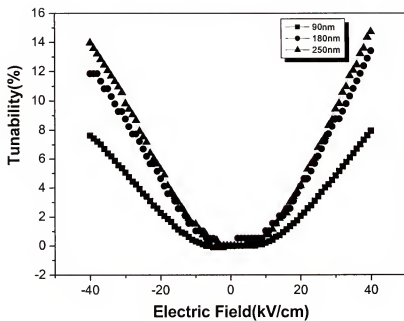


Figure 7-7. The extracted intrinsic tunability of the KTN:Ti films as a function of electric field with different film thicknesses

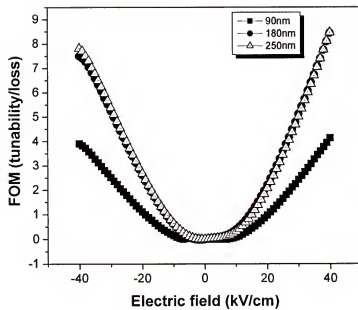


Figure 7-8. FOM of KTN:Ti films as a function of electric field with different film thicknesses

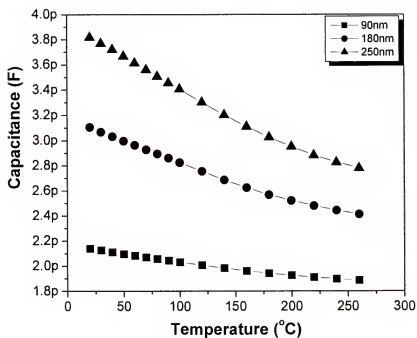


Figure 7-9. Capacitance results of KTN:Ti film grown at 750°C and 100mTorr oxygen ambient on (001) MgO substrate as a function of capacitance measurement temperature

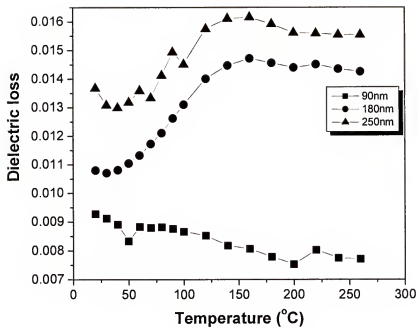


Figure 7-10. Dielectric loss of KTN:Ti film as a function of capacitance measurement temperatures under different film thicknesses

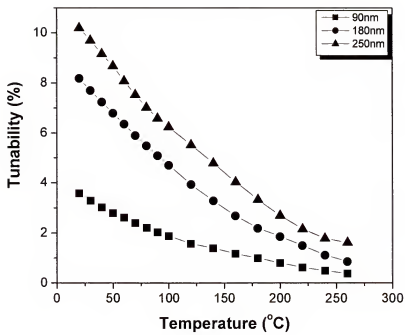


Figure 7-11. Tunability of KTN:Ti film as a function of capacitance measurement temperatures under different film thicknesses

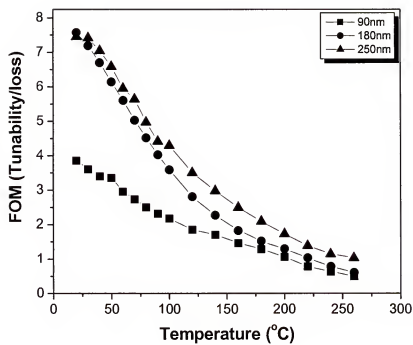


Figure 7-12. FOM of KTN:Ti film as a function of capacitance measurement temperatures under different film thicknesses

CHAPTER 8

SUMMARY

KTaO_3 , KNbO_3 and solid solution $\text{K}(\text{Ta,Nb})\text{O}_3$ are very interesting materials with wide application areas because of their unique electric properties. The first part of the research was focused to achieve an atomically flat surface with a unit cell step height on the surface of a (001) KTaO_3 single crystal. The combination of etching and annealing of (001) KTaO_3 removed effectively the surface potassium hydroxide, and reconstructed the surface via annealing. Surface steps were observed at the condition of 15 min etching in BOE and then followed by annealing in air at 700°C for 3 or 4hrs. However, longer etching times and higher annealing temperatures caused a roughening of the surface and the formation of particulates on the surface of the KTaO_3 (100) face.

The second part of the research was to fabricate a semiconducting KTaO_3 film by cation and defect doping to use as a channel in epitaxial FET devices. However, unlike SrTiO_{3-x} , semiconducting behavior was not shown for the films grown in vacuum. Nevertheless, epitaxially grown $\text{KTaO}_3\text{:Ca}$ films grown at 30 mTorr partial pressure of 96% Ar / 4% H_2 atmosphere and 700°C growth temperature were semiconducting. The resistivity of the $\text{KTaO}_3\text{:Ca}$ film was $10.4\ \Omega\text{cm}$ at room temperature and showed n-type semiconducting behavior.

The third part of the research was investigating dielectric properties of Ti doped $\text{K}(\text{Ta,Nb})\text{O}_3$ thin films for tunable microwave applications. For this purpose, growth conditions, thickness, and annealing conditions of $\text{KTN}:\text{Ti}$ films were investigated.

To achieve optimal growth conditions, KTN:Ti films were grown at different oxygen partial pressures. KTN:Ti film grown in vacuum at 750°C showed high tunability. However, this film also had a high loss tangent due to oxygen vacancies. KTN:Ti films grown at oxygen pressure of 100mTorr and growth temperature of 750°C had a better figure of merit compared to films grown under other conditions. This film showed 10% tunability at a 40kV/cm electric field, 1 MHz frequency, and at room temperature. Its loss tangent was around 0.02. Compared to an undoped KTN film, a Ti doped KTN film has a lower loss tangent and is temperature independent by trapping electrons effectively.

For a thickness effect for dielectric properties of a KTN:Ti film, the KTN:Ti films were synthesized at 100mTorr and 750°C with different film thickness. Due to size effect, thinner KTN:Ti films showed a smaller tunability and loss tangent than thicker films. However, the figure of merit of KTN:Ti film was larger in a thicker KTN:Ti film.

The dielectric properties of Ti doped KTN films were studied by annealing in oxygen ambient. The annealing treatment of KTN:Ti films significantly influenced the dielectric properties. As-deposited KTN:Ti films showed relatively high dielectric loss due to oxygen vacancies. However, KTN:Ti films annealed at 900°C for 2hrs in oxygen had a lower dielectric loss and tunability at room temperature, 0.0027, and 3.8%, respectively. The figure of merits (FOM) of annealed KTN:Ti film had higher values in all of the measurement temperature ranges than that of unannealed KTN:Ti film.

LIST OF REFERENCES

- 1 Gutmann R, Hulliger J, and Wuest H, "Growth of paraelectric and ferroelectric epitaxial layers of $\text{KTa}_{1-x}\text{Nb}_x\text{O}_3$ by liquid-phase epitaxy," *Ferroelectrics* 1992; **134**: 291-296.
- 2 Gutmann R, Hulliger J, and Reusser E, "Liquid-phase epitaxy of lattice-matched $\text{KTa}_{1-x}\text{Nb}_x\text{O}_3$ grown on KTaO_3 substrate," *Journal of Crystal Growth* 1993; **126**: 578-588.
- 3 Wang SM, Li ZY, Zhang DM, Zhang GS, Sun JM, and Zheng P, "Dielectric, ferroelectric properties of $\text{KTa}_{0.65}\text{Nb}_{0.35}\text{O}_3$ thin films prepared by sol-gel process on $\text{Pt}(111)/\text{Ti}/\text{MgO}(100)$ substrates," *Journal of Sol-Gel Science and Technology* 2000; **17**: 159-162.
- 4 Gust MC, Evans ND, Momoda LA, and McCartney ML, "In-situ transmission electron microscopy crystallization studies of sol-gel-derived barium titanate thin films," *Journal of the American Ceramic Society* 1997; **80**: 2828-2836.
- 5 Park BE, and Ishiwara H, "Fabrication of PZT films on Si substrates by sol-gel method using Y_2O_3 buffer layers," *Integrated Ferroelectrics* 2001; **33**: 109-116.
- 6 Lee DG, Jang JH, Kim JJ, Cho SH, and Lee HY, "Ferroelectric properties of SBN thin films deposited by ion beam sputtering," *Ferroelectrics* 2004; **304**: 1003-1007.
- 7 Auciello O, Gifford KD, Lichtenwalner DJ, Dat R, Alshareef HN, Bellur KR, and Kington AI, "A review of composition-structure-property relationships for Pzt-based heterostructure capacitors," *Integrated Ferroelectrics* 1995; **6**: 173-187.
- 8 Imada S, Shouriki S, Tokumitsu E, and Ishiwara H, "Epitaxial growth of ferroelectric YMnO_3 thin films on Si (111) substrates by molecular beam epitaxy," *Japanese Journal of Applied Physics Part 1-Regular Papers Short Notes & Review Papers* 1998; **37**: 6497-6501.
- 9 Jiang JC, Pan XQ, Tian W, Theis CD, and Schlom DG, "Abrupt $\text{PbTiO}_3/\text{SrTiO}_3$ superlattices grown by reactive molecular beam epitaxy," *Applied Physics Letters* 1999; **74**: 2851-2853.
- 10 Yoneda Y, Sakaue K, and Terauchi H, "RHEED observation of BaTiO_3 thin films grown by MBE," *Surface Science* 2003; **529**: 283-287.

- 11 Yoneda Y, Okabe T, Sakaue K, and Terauchi H, "Growth of perovskite type thin films by MBE," *Journal of the Korean Physical Society* 1996; **29**: S652-S655.
- 12 Christen HM, Boatner LA, Budai JD, Chisholm MF, Gea L A, Marrero PJ, and Norton DP, "The growth and properties of epitaxial KNbO_3 thin films and $\text{KNbO}_3/\text{KTaO}_3$ superlattices," *Applied Physics Letters* 1996; **68**: 1488-1490.
- 13 Otani Y, Okamura S, and Shiosaki T, "Recent developments on MOCVD of ferroelectric thin films," *Journal of Electroceramics* 2004; **13**: 15-22.
- 14 Huang SS, Liu JL, and Wu TB, "Thickness dependent characteristics in the growth of $\text{Pb}(\text{Zr}_{0.4}\text{Ti}_{0.6})\text{O}_3$ thin films on LaNiO_3 electrode by MOCVD," *Integrated Ferroelectrics* 2004; **68**: 53-62.
- 15 Romanov MV, Korsakov IE, Kaul AR, Stefanovich SY, Bolshakov IA, and Wahl G, "MOCVD of KNbO_3 ferroelectric films and their characterization," *Chemical Vapor Deposition* 2004; **10**: 318-324.
- 16 Funakubo H, "Recent development in the preparation of ferroelectric thin films by MOCVD," *Ferroelectric Random Access Memories Fundamentals and Applications*, 2004, vol 93, pp 95-103.
- 17 Dubourdieu C, Pantou R, Weiss F, Senateur JP, Dooryhee E, Hodeau JL, Nemoz M, Kobernik G, and Haessler W, "Structural and dielectric properties of $(\text{BaTiO}_3/\text{SrTiO}_3)$ superlattices grown by MOVCD," *Ferroelectrics* 2002; **268**: 557-562.
- 18 Shimizu M, Fujisawa H, Niu H, and Honda K, "Growth of ferroelectric $\text{PbZr}_x\text{Ti}_{1-x}\text{O}_3$ thin films by metalorganic chemical vapor deposition (MOCVD)," *Journal of Crystal Growth* 2002; **237**: 448-454.
- 19 Jeon YA, Choi ES, Seo TS, and Yoon SG, "Improvements in tunability of $(\text{Ba}_{0.5}\text{Sr}_{0.5})\text{TiO}_3$ thin films by use of metalorganic chemical vapor deposited $(\text{Ba,Sr})\text{RuO}_3$ interfacial layers," *Applied Physics Letters* 2001; **79**: 1012-1014.
- 20 Dalberth MJ, Stauber RE, Price JC, Rogers CT, and Galt D, "Improved low frequency and microwave dielectric response in strontium titanate thin films grown by pulsed laser ablation," *Applied Physics Letters* 1998; **72**: 507-509.
- 21 Xu J, Menesklou W, and Ivers-Tiffée E, "Processing and properties of BST thin films for tunable microwave devices," *Journal of the European Ceramic Society* 2004; **24**: 1735-1739.
- 22 Bouzehouane K, Woodall P, Marcilhac B, Khodan AN, Crete D, Jacquet E, Mage JC, and Contour JP, "Enhanced dielectric properties of SrTiO_3 epitaxial thin film for tunable microwave devices," *Applied Physics Letters* 2002; **80**: 109-111.

- 23 Kubo M, Oumi Y, Miura R, Stirling A, Miyamoto A, Kawasaki M, Yoshimoto M, and Koinuma H, "Atomic control of layer-by-layer epitaxial growth on $\text{SrTiO}_3(001)$: Molecular-dynamics simulations," *Physical Review B* 1997; **56**: 13535-13542.
- 24 Kawasaki M, Ohtomo A, Arakane T, Takahashi K, Yoshimoto M, and Koinuma H, "Atomic control of SrTiO_3 surface for perfect epitaxy of perovskite oxides," *Applied Surface Science* 1996; **107**: 102-106.
- 25 Ohnishi T, Takahashi K, Nakamura M, Kawasaki M, Yoshimoto M, and Koinuma H, "A-site layer terminated perovskite substrate: NdGaO_3 ," *Applied Physics Letters* 1999; **74**: 2531-2533.
- 26 Jantunen H, Hu T, Uusimäki A, and Leppavuori S, "Tape casting of ferroelectric, dielectric, piezoelectric and ferromagnetic materials," *Journal of the European Ceramic Society* 2004; **24**: 1077-1081.
- 27 Yue W, and Yi-jian J, "Crystal orientation dependence of piezoelectric properties in LiNbO_3 and LiTaO_3 ," *Optical Materials* 2003; **23**: 403-408.
- 28 Tian J, Zhang Q, Zhou Q, Yoon SF, Ahn J, Wang SG, Li JQ, and Yang DJ, "Study of well adherent DLC film deposited on piezoelectric LiTaO_3 substrate," *Applied Surface Science* 2005; **239**: 255-258.
- 29 Meunier C, Munnik F, Germann E, Schluechter R, Pujol MD, Kondratiev SN, and Mikhailov S, "DLC films on LiTaO_3 for SAW devices," *Surface and Coatings Technology* 2004; **180-181**: 234-237.
- 30 Munoz-Saldana J, Schneider GA, and Eng LM, "Stress induced movement of ferroelastic domain walls in BaTiO_3 single crystals evaluated by scanning force microscopy," *Surface Science* 2001; **480**: L402-L410.
- 31 Xu Q, Chen S, Chen W, Wu S, Lee J, Zhou J, Sun H, and Li Y, "Structure, piezoelectric properties and ferroelectric properties of $(\text{Na}_{0.5}\text{Bi}_{0.5})_{1-x}\text{Ba}_x\text{TiO}_3$ system," *Journal of Alloys and Compounds* 2004; **381**: 221-225.
- 32 Hou YD, Zhu MK, Wang H, Wang B, Tian CS, and Yan H, "Effects of atmospheric powder on microstructure and piezoelectric properties of PMZN-PZT quaternary ceramics," *Journal of the European Ceramic Society* 2004; **24**: 3731-3737.
- 33 Chen BH, Huang CL, and Wu L, "Promotion of piezoelectric properties of lead zirconate titanate ceramics with (Zr,Ti) partially replaced by Nb_2O_5 ," *Solid-State Electronics* 2004; **48**: 2293-2297.

- 34 Ng SY, and Boccaccini AR, "Lead zirconate titanate films on metallic substrates by electrophoretic deposition," *Materials Science and Engineering B* 2005; **116**: 208-214.
- 35 Lee S, Tanaka T, Inoue K, Kim JM, Shin YE, and Okuyama M, "Stress influences on the ultrasonic transducers," *Sensors and Actuators A: Physical*; **In Press**, **Corrected Proof**.
- 36 Feng C, and Xu P, "The detection mechanism of LiTaO_3 type II pyroelectric detectors.: II. The tertiary pyroelectric effect," *Infrared Physics & Technology* 1999; **40**: 71-78.
- 37 Mendes RG, and Eiras JA, "Influence of neodymium and lanthanum doping in the pyroelectric properties of strontium barium niobate (SBN) thin films," *Journal of the European Ceramic Society* 2004; **24**: 1637-1640.
- 38 Amorin H, Guerrero F, Portelles J, Gonzalez I, Fundora A, Siqueiros J, and Valenzuela J, "Effect of La^{3+} doping on the polarization of the LSBN ceramic system," *Solid State Communications* 1998; **106**: 555-558.
- 39 Wu NJ, Xu YQ, Ritums D, Chen YS, and Ignatiev A, "Pyroelectric/superconducting oxide heterostructures for uncooled wide-band infrared detection," *Physica C: Superconductivity* 2000; **341-348**: 2743-2744.
- 40 Callister WD, "Materials science and engineering : an introduction," New York, John Wiley & Sons, INC., 1985.
- 41 Christen HM, Norton DP, Gea LA, and Boatner LA, "Pulsed laser deposition of solid-solution films using segmented targets," *Thin Solid Films* 1998; **312**: 156-159.
- 42 Fujii Y, and Sakudo T, "Dielectric and optical-properties of KTaO_3 ," *Journal of the Physical Society of Japan* 1976; **41**: 888-893.
- 43 Triebwasser S, and Holtzberg F, "Ferroelectric behavior of solid solutions of KNbO_3 and KTaO_3 ," *Physical Review* 1955; **98**: 1201-1201.
- 44 Triebwasser S, "Study of ferroelectric transitions of solid-solution single crystals of KNbO_3 - KTaO_3 ," *Physical Review* 1959; **114**: 63-70.
- 45 Samara GA, "Glasslike behavior and novel pressure effects in $\text{KTa}_{1-x}\text{Nb}_x\text{O}_3$," *Physical Review Letters* 1984; **53**: 298-301.
- 46 Rytz D, Chatelain A, and Hochli UT, "Elastic properties in quantum ferroelectric $\text{KTa}_{1-x}\text{Nb}_x\text{O}_3$," *Physical Review B* 1983; **27**: 6830-6840.

- 47 von Hippel AR, "Dielectrics and waves," New York, John Wiley & Sons, Inc., 1954.
- 48 Barsoum MW, "Fundamentals of ceramics," McGraw-Hill, 1997.
- 49 Gevorgian S, Carlsson E, Rudner S, Wernlund LD, Wang X, and Helmersson U, "Modelling of thin-film HTS/ferroelectric interdigital capacitors," *Iee Proceedings-Microwaves Antennas and Propagation* 1996; **143**: 397-401.
- 50 Cheng YL, Wang Y, Chan HLW, and Choy CL, "Preparation and characterization of (Ba, Sr)TiO₃ thin films using interdigital electrodes," *Microelectronic Engineering* 2003; **66**: 872-879.
- 51 Wang Y, Chong N, Cheng YL, Chan HLW, and Choy CL, "Dependence of capacitance on electrode configuration for ferroelectric films with interdigital electrodes," *Microelectronic Engineering* 2003; **66**: 880-886.
- 52 Cheng YL, Chong N, Wang Y, Liu JZ, Chan HLW, and Choy CL, "Microwave characterization of BST thin films on LAO interdigital capacitor," *Integrated Ferroelectrics* 2003; **55**: 939-946.
- 53 Shaw TM, Trolrier-McKinstry S, and McIntyre PC, "The properties of ferroelectric films at small dimensions," *Annual Review of Materials Science* 2000; **30**: 263-298.
- 54 Tuttle BA, Desu SB, Ramesh R, and Shiosaki T, *Materials Research Society Symposium Proceeding* 1995; **361**: 515.
- 55 Delage T, Champeaux C, Catherinot A, Seaux JF, Madrangeas V, and Cros D, "High-K BST films deposited on MgO by PLD with and without buffer-layer," *Thin Solid Films* 2004; **453-454**: 279-284.
- 56 Wang TS, Duan XF, Hu WF, Liu W, Li L, Peng W, and Chen YF, "Electron microscopy of step-flow grown c-axis YBa₂Cu₃O_{7- δ} thin films on vicinal substrates," *Superconductor Science & Technology* 2002; **15**: 1199-1202.
- 57 Nelson CE, "Ferrite-Tunable Microwave Cavities and the Introduction of a New Reflectionless, Tunable Microwave Filter," *Proceedings of the Institute of Radio Engineers* 1956; **44**: 1449-1455.
- 58 Bobyl A, Suris R, Karmanenko S, Semenov A, Melkov A, Konuhov S, and Olshevski A, "The ferrite/superconductor layered structure for tunable microwave device," *Physica C-Superconductivity and Its Applications* 2002; **372**: 508-510.

- 59 Rijnders G, Koster G, Blank DHA, and Rogalla H, "In-situ monitoring during PLD of $\text{YBa}_2\text{Cu}_3\text{O}_{7-\delta}$ using RHEED at high oxygen pressure," *Ieee Transactions on Applied Superconductivity* 1999; **9**: 1547-1550.
- 60 Rijnders G, Koster G, Blank DHA, and Rogalla H, "In-situ growth monitoring during PLD of oxides using RHEED at high oxygen pressure," *Materials Science and Engineering B-Solid State Materials for Advanced Technology* 1998; **56**: 223-227.
- 61 Suzuki Y, "Epitaxial spinel ferrite thin films," *Annual Review of Materials Research* 2001; **31**: 265-289.
- 62 Saenger KL, Roy RA, Etzold KF, and Cuomo JJ, "Lead zirconate titanate films produced by pulsed laser deposition," *Materials Research Society Symposium* 1990; **200**: 115-200.
- 63 Chrisey DB, and K. HG, "Pulsed Laser Deposition of Thin Films," New York, John Wiley & Sons, INC., 1994.
- 64 Hummel RE, "Electronic Properties of Materials," New York, Springer, 1992.
- 65 Ready JF, "Development of Plume of Material Vaporized by Giant-Pulse Laser," *Applied Physics Letters* 1963; **3**: 11-13.
- 66 Schwarz H, and Tourtell.H, "Vacuum deposition by high-energy laser with emphasis on barium titanate films," *Journal of Vacuum Science & Technology* 1969; **6**: 373-&.
- 67 Schlom DG, Hellman ES, Hartford EH, Eom CB, Clark JC, and Mannhart J, "Origin of the phi approximate to +/-9 degrees peaks in $\text{YBa}_2\text{Cu}_3\text{O}_{7-\delta}$ films grown on cubic zirconia substrates," *Journal of Materials Research* 1996; **11**: 1336-1348.
- 68 Azaroff LV, "Elements of X-ray crystallography," New York, McGraw-Hill, 1968.
- 69 Van der Pauw LJ, "A method of measuring the resistivity and hall coefficient on lamellae of arbitrary shape," *Philips Research Report* 1958; **13**.
- 70 Noudem JG, Hassini A, Gervais M, and Gervais F, "Processing and physical properties of $\text{La}_{0.8-z}\text{Y}_z\text{Sr}_{0.2}\text{MnO}_3$ bulk, thick films and single crystal," *Solid State Sciences* 2003; **5**: 1001-1007.
- 71 Wang HS, Liu YW, Ma K, Peng ZQ, Cui DF, Lu HB, Zhou YL, Chen ZH, Li L, and Yang GZ, "Structural and ferroelectric properties of $\text{BaTiO}_3/\text{YBa}_2\text{Cu}_3\text{O}_7$

- heterostructures prepared by laser molecular beam epitaxy," *Physica C* 1997; **282**: 699-700.
- 72 Woodall P, Bouzehouane K, Marcilhac B, Crete DG, Jacquet E, Mage JC, and Contour JP, "Epitaxial $\text{YBa}_2\text{Cu}_3\text{O}_{7-\delta}/\text{SrTiO}_3$ heterostructures grown on LaAlO_3 substrate by pulsed laser deposition for voltage tunable microwave filter applications," *Ieee Transactions on Applied Superconductivity* 2001; **11**: 1150-1153.
 - 73 Choi J, Kim E, Park SY, Lee JS, Sung TH, Park Y, and No K, "Fabrication and characterization of $\text{Ba}_x\text{Sr}_{1-x}\text{TiO}_3/\text{YBa}_2\text{Cu}_3\text{O}_{7-x}/\text{SrTiO}_3$ structure," *Japanese Journal of Applied Physics Part 1-Regular Papers Short Notes & Review Papers* 2002; **41**: 5567-5571.
 - 74 Jia QX, Findikoglu AT, Arendt P, Foltyn SR, Roper JM, Groves JR, Coulter JY, Li YQ, and Dionne GF, "Superconducting $\text{YBa}_2\text{Cu}_3\text{O}_{7-x}$ thin films on polycrystalline ferrite for magnetically tunable microwave components," *Applied Physics Letters* 1998; **72**: 1763-1765.
 - 75 Chen WK, Cheng CM, Huang JY, Hsieh WF, and Tseng TY, "Study of linear and nonlinear optical properties of distorted Ti-O₆ perovskite structure in $\text{Ba}_x\text{Sr}_{1-x}\text{TiO}_3$," *Journal of Physics and Chemistry of Solids* 2000; **61**: 969-977.
 - 76 Lippmaa M, Kawasaki M, Ohtomo A, Sato T, Iwatsuki M, and Koinuma H, "Observation of SrTiO_3 step edge dynamics by real-time high-temperature STM," *Applied Surface Science* 1998; **132**: 582-586.
 - 77 Lippmaa M, Takahashi K, Ohtomo A, Ohashi S, Ohnishi T, Nakagawa N, Sato T, Iwatsuki M, Koinuma H, and Kawasaki M, "Atom technology for Josephson tunnel junctions: SrTiO_3 substrate surface," *Materials Science and Engineering B-Solid State Materials for Advanced Technology* 1998; **56**: 111-116.
 - 78 Kawasaki M, Takahashi K, Maeda T, Tsuchiya R, Shinohara M, Ishiyama O, Yonezawa T, Yoshimoto M, and Koinuma H, "Atomic control of the SrTiO_3 crystal surface," *Science* 1994; **266**: 1540-1542.
 - 79 Rijnders G, Koster G, Leca V, Blank DHA, and Rogalla H, "Imposed layer-by-layer growth with pulsed laser interval deposition," *Applied Surface Science* 2000; **168**: 223-226.
 - 80 Koster G, Rijnders G, Blank DHA, and Rogalla H, "Surface morphology determined by (001) single-crystal SrTiO_3 termination," *Physica C-Superconductivity and Its Applications* 2000; **339**: 215-230.
 - 81 Kubo T, and Nozoye H, "Surface structure of $\text{SrTiO}_3(100)$," *Surface Science* 2003; **542**: 177-191.

- 82 Koster G, Kropman BL, Rijnders G, Blank DHA, and Rogalla H, "Quasi-ideal strontium titanate crystal surfaces through formation of strontium hydroxide," *Applied Physics Letters* 1998; **73**: 2920-2922.
- 83 Maeda T, Lee GH, Ohnishi T, Kawasaki M, Yoshimoto M, and Koinuma H, "Molecular layer-by-layer growth of SrTiO_3 and BaTiO_3 films by laser molecular beam epitaxy," *Materials Science and Engineering B-Solid State Materials for Advanced Technology* 1996; **41**: 134-137.
- 84 Hewat AW, "Soft modes and structure, spontaneous polarization and curie constants of perovskite ferroelectrics-tetragonal potassium niobate," *Journal of Physics C-Solid State Physics* 1973; **6**: 1074-1084.
- 85 Cai WZ, Shastri S, Grivna G, Wu YJ, and Loecheit G, "RF characteristics of a high-performance, 10-fF/ μm^2 capacitor in a deep trench," *Ieee Electron Device Letters* 2004; **25**: 468-470.
- 86 Christen HM, Boatner LA, Budai JD, Chisholm MF, Gerber C, and Urbanik M, "Semiconducting epitaxial films of metastable $\text{SrRu}_{0.5}\text{Sn}_{0.5}\text{O}_3$ grown by pulsed laser deposition," *Applied Physics Letters* 1997; **70**: 2147-2149.
- 87 Chow AF, Lichtenwalner DJ, Woolcott RR, Graettinger TM, Auciello O, Kingon AI, Boatner LA, and Parikh NR, "Epitaxial KNbO_3 thin-films on KTaO_3 , MgAl_2O_4 , and MgO substrates," *Applied Physics Letters* 1994; **65**: 1073-1075.
- 88 Naito M, Karimoto S, and Tsukada A, "Epitaxy-stabilized n-type superconducting cuprates," *Superconductor Science & Technology* 2002; **15**: 1663-1668.
- 89 Kim Y, Erbil A, and Boatner LA, "Substrate dependence in the growth of epitaxial $\text{Pb}_{1-x}\text{La}_x\text{TiO}_3$ thin films," *Applied Physics Letters* 1996; **69**: 2187-2189.
- 90 Prusseit W, Boatner LA, and Rytz D, "Epitaxial $\text{YBa}_2\text{Cu}_3\text{O}_7$ growth on KTaO_3 (001) single-crystals," *Applied Physics Letters* 1993; **63**: 3376-3378.
- 91 Szot K, Speier W, Pawelczyk M *et al*: Chemical inhomogeneity in the near-surface region of KTaO_3 evolving at elevated temperatures. *Journal of Physics-Condensed Matter* 2000; **12**: 4687-4697.
- 92 Galasso FS, "Perovskites and high T_c superconductors," New York, Gordon and Breach, 1990.
- 93 Cerda J, Arbiol J, Dezanneau G, Diaz R, and Morante JR, "Perovskite-type BaSnO_3 powders for high temperature gas sensor applications" *Sensors and Actuators B-Chemical* 2002; **84**: 21-25.

- 94 Huang K, Wan J, and Goodenough JB, "Oxide-ion conducting ceramics for solid oxide fuel cells," *Journal of Materials Science* 2001; **36**: 1093-1098.
- 95 Aggarwal S, Ganpule C, Jenkins IG, Nagaraj B, Stanishevsky A, Melngailis J, Williams E, and Ramesh R, "High density ferroelectric memories: Materials, processing and scaling," *Integrated Ferroelectrics* 2000; **29**: 213-225.
- 96 Marre D, Bellingeri E, Pellicchi I, Pellegrino L, Tumino A, and Siri AS, "Electronic devices based on semiconducting strontium titanate," *Journal De Physique Iv* 2001; **11**: 331-335.
- 97 Toulouse J, Wang XM, Knauss LA, and Boatner LA, "Dielectric nonlinearity and spontaneous polarization of $\text{KTa}_{1-x}\text{Nb}_x\text{O}_3$ in the diffuse transition range," *Physical Review B* 1991; **43**: 8297-8302.
- 98 Bozinis DG, and Hurrell JP, "Optical modes and dielectric properties of ferroelectric orthorhombic KNbO_3 ," *Physical Review B* 1976; **13**: 3109-3120.
- 99 Tsukioka M, Tanaka J, and Miyazawa Y, "Electrical-conduction mechanism in semiconducting KTaO_3 ," *Journal of the Physical Society of Japan* 1979; **46**: 1785-1791.
- 100 Deputy GO, and Vest RW, "Defect structure and electrical-properties of KTaO_3 ," *Journal of the American Ceramic Society* 1978; **61**: 321-325.
- 101 Wemple SH, "Some transport properties of oxygen-deficient single-crystal potassium tantalate (KTaO_3)," *Physical Review* 1965; **137**: 1575-&.
- 102 Baer WS, "Interband faraday rotation in some perovskite oxides and rutile," *Journal of Physics and Chemistry of Solids* 1967; **28**: 677-&.
- 103 Johnson KW, and Olson DH, "Electron tunneling into KTaO_3 schottky barrier junctions," *Physical Review B* 1971; **3**: 1244-&.
- 104 Sroubek Z, "Electron tunneling and band structure of SrTiO_3 and KTaO_3 ," *Physical Review B* 1970; **2**: 3170.
- 105 Sasaki Y, Fujii I, Matsui T, and Morii K, "Influence of antimony doping on electrical properties of barium titanate (BaTiO_3) thin films," *Materials Letters* 1996; **26**: 265-271.
- 106 Lemee N, Dubourdieu C, Delabouglise G, Senateur JP, and Laroudie F, "Semiconductive Nb-doped BaTiO_3 films grown by pulsed injection metalorganic chemical vapor deposition," *Journal of Crystal Growth* 2002; **235**: 347-351.

- 107 Goto Y, and Kachi S, "Studies on mechanism of electric conduction in Fe-doped BaTiO₃ single crystals by applying Kerr effect," *Journal of Physics and Chemistry of Solids* 1971; **32**: 889-895.
- 108 GrosseHolz KO, Cillessen JFM, and Waser R, "Electrical characterization of semiconducting La doped SrTiO₃ thin films prepared by pulsed laser deposition," *Applied Surface Science* 1996; **96-8**: 784-790.
- 109 Wang HH, Cui DF, Dai SY, Lu HB, Zhou YL, Chen ZH, and Yang GZ, "Optical and transport properties of Sb-doped SrTiO₃ thin films," *Journal of Applied Physics* 2001; **90**: 4664-4667.
- 110 Yilmaz S, Venkatesan T, and Gerhardmulhaupt R, "Pulsed laser deposition of stoichiometric potassium-tantalate-niobate films from segmented evaporation targets," *Applied Physics Letters* 1991; **58**: 2479-2481.
- 111 Gim Y, Hudson T, Fan Y, Kwon C, Findikoglu AT, Gibbons BJ, Park BH, and Jia QX, "Microstructure and dielectric properties of Ba_{1-x}Sr_xTiO₃ films grown on LaAlO₃ substrates," *Applied Physics Letters* 2000; **77**: 1200-1202.
- 112 Katayama I, Shirai M, and Tanaka K, "High-frequency nonlinear microwave response in quantum paraelectric potassium tantalite," *Journal of Luminescence* 2003; **102**: 54-59.
- 113 Im J, Auciello O, Baumann PK, Streiffer SK, Kaufman DY, and Krauss AR, "Composition-control of magnetron-sputter-deposited (Ba_xSr_{1-x})Ti_{1+y}O_{3+z} thin films for voltage tunable devices," *Applied Physics Letters* 2000; **76**: 625-627.
- 114 Padmini P, Taylor TR, Lefevre MJ, Nagra AS, York RA, and Speck JS, "Realization of high tunability barium strontium titanate thin films by rf magnetron sputtering," *Applied Physics Letters* 1999; **75**: 3186-3188.
- 115 Sengupta LC, and Sengupta S, "Novel ferroelectric materials for phased array antennas," *Ieee Transactions on Ultrasonics Ferroelectrics and Frequency Control* 1997; **44**: 792-797.
- 116 Babbitt RW, Koscica TE, and Drach WC, "Planar microwave electrooptic phase shifters," *Microwave Journal* 1992; **35**: 63.
- 117 Belokopytov GV, Ivanov IV, Katanov SI, Moiseev NN, and Syrnikov PP, "Dielectric losses of potassium tantalate crystals at 0.5-15 Ghz frequencies," *Fizika Tverdogo Tela* 1982; **24**: 1865-1867.
- 118 Carter AC, Horwitz JS, Chrisey DB, Pond JM, Kirchoefer SW, and Chang WT, "Pulsed laser deposition of ferroelectric thin films for room temperature active microwave electronics," *Integrated Ferroelectrics* 1997; **17**: 273-285.

- 119 Fontana MD, Metrat G, Servoin JL, and Gervais F, "Infrared-spectroscopy in KNbO_3 through the successive ferroelectric phase-transitions," *Journal of Physics C-Solid State Physics* 1984; **17**: 483-514.
- 120 Dubernet P, Ravez J, and Pigram A, "Densification and frequency dielectric response (10^2 to 10^9Hz) of ferroelectric $\text{K}(\text{Ta}_{0.5}\text{Nb}_{0.5})\text{O}_3$ ceramics," *Physica Status Solidi a-Applied Research* 1995; **152**: 555-562.
- 121 Christen HM, Specht ED, Norton DP, Chisholm MF, and Boatner LA, "Long-range ferroelectric interactions in $\text{KTaO}_3/\text{KNbO}_3$ superlattice structures," *Applied Physics Letters* 1998; **72**: 2535-2537.
- 122 Jain M, Majumder SB, Katiyar RS, Miranda FA, and Van Keuls FW, "Improvement in electrical characteristics of graded manganese doped barium strontium titanate thin films," *Applied Physics Letters* 2003; **82**: 1911-1913.
- 123 Cole MW, Joshi PC, and Ervin MH, "La doped $\text{Ba}_{1-x}\text{Sr}_x\text{TiO}_3$ thin films for tunable device applications," *Journal of Applied Physics* 2001; **89**: 6336-6340.
- 124 Kim HS, Lim MH, Kim HG, and Kim ID, "Characterization of Ni-doped BST thin films on LSCO buffer layers prepared by pulsed laser deposition," *Electrochemical and Solid State Letters* 2004; **7**: J1-J3.
- 125 Samara GA, and Boatner LA, "Ferroelectric-to-relaxor crossover and oxygen vacancy hopping in the compositionally disordered perovskites $\text{KTa}_{1-x}\text{Nb}_x\text{O}_3\text{:Ca}$," *Physical Review B* 2000; **61**: 3889-3896.
- 126 Bitton G, Feldman Y, and Agranat AJ, "Relaxation processes of off-center impurities in KTN:Li crystals," *Journal of Non-Crystalline Solids* 2002; **305**: 362-367.
- 127 Pattnaik RK, and Toulouse J, "Influence of orientational relaxation on the electrostrictive coupling in $\text{K}_{1-x}\text{Li}_x\text{TaO}_3$," *Journal of Physics and Chemistry of Solids* 2000; **61**: 251-259.
- 128 Ioachim A, Toacsan MI, Banciu MG, Nedelcu L, Plapcianu C, Alexandru H, Berbecaru C, Ghetu D, Stoica G, and Ramer R, "Frequency agile BST materials for microwave applications," *Journal of Optoelectronics and Advanced Materials* 2003; **5**: 1389-1393.
- 129 Lee SJ, Moon SE, Kwak MH, Ryu HC, Kim YT, and Kang KY, "High dielectric tunability of $(\text{Ba}, \text{Sr})\text{TiO}_3$ thin films and their coplanar waveguide phase shifter applications," *Japanese Journal of Applied Physics Part 1-Regular Papers Short Notes & Review Papers* 2004; **43**: 6750-6754.

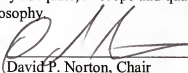
- 130 Lee BT, and Hwang CS, "Influences of interfacial intrinsic low-dielectric layers on the dielectric properties of sputtered (Ba,Sr)TiO₃ thin films," *Applied Physics Letters* 2000; **77**: 124-126.
- 131 Hyun S, and Char K, "Effects of strain on the dielectric properties of tunable dielectric SrTiO₃ thin films," *Applied Physics Letters* 2001; **79**: 254-256.
- 132 Basceri C, Streiffer SK, Kingon AI, and Waser R, "The dielectric response as a function of temperature and film thickness of fiber-textured (Ba,Sr)TiO₃ thin films grown by chemical vapor deposition," *Journal of Applied Physics* 1997; **82**: 2497-2504.
- 133 Abe K, and Komatsu S, "Measurement and thermodynamic analyses of the dielectric-constant of epitaxially grown SrTiO₃ Films," *Japanese Journal of Applied Physics Part 2-Letters* 1993; **32**: L1157-L1159.
- 134 Zhou C, and News DM, "Intrinsic dead layer effect and the performance of ferroelectric thin film capacitors," *Journal of Applied Physics* 1997; **82**: 3081-3088.
- 135 Natori K, Otani D, and Sano N, "Thickness dependence of the effective dielectric constant in a thin film capacitor," *Applied Physics Letters* 1998; **73**: 632-634.
- 136 Bae HJ, Sigman J, Norton DP, and Boatner L, "Dielectric properties of Ti-doped K(Ta,Nb)O₃ thin films grown by pulsed laser deposition," *Materials Science and Engineering B* 2005; **117**: 87-91.

BIOGRAPHICAL SKETCH

Hyung-jin Bae was born in Seoul, Korea, on January 4th, 1972. He earned his Bachelor of Science in metallurgical engineering in In-ha University, Incheon, Korea, in 1996. And he worked in LG Electronics for one year. With working experience in the field, he decided to pursue his study. He earned a Master of Science in metallurgical engineering with specialty of electronic materials (especially, the thermal stability of Ta-Si-N and Nb-Si-N as a diffusion barrier between Cu and Si) in In-ha University, Incheon, Korea, in 1999.

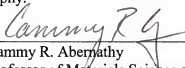
He moved to the USA in March 1999. He studied English as a second language at the University of Idaho, Moscow. While learning English, he prepared and applied to several graduate schools in the USA including the University of Florida. He started graduate school in material science and engineering, University of Florida, in Aug. 1999. He joined Dr. Norton's research group to pursue a Doctor of Philosophy degree in Jan. 2001. His interest area for his research was oxide electronic materials, which could be applied in various areas such as FRAM, tunable microwave devices, and phase shifter, and wireless communication devices. During his research, he learned how to synthesize targets and films, and understand equipment and vacuum system by building UHV laser MBE. After graduation, he plans to pursue a job in the USA.

I certify that I have read this study and that in my opinion it conforms to acceptable standards of scholarly presentation and is fully adequate, in scope and quality, as a dissertation for the degree of Doctor of Philosophy.



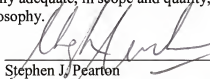
David P. Norton, Chair
Professor of Materials Science and
Engineering

I certify that I have read this study and that in my opinion it conforms to acceptable standards of scholarly presentation and is fully adequate, in scope and quality, as a dissertation for the degree of Doctor of Philosophy.



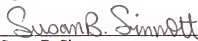
Cammy R. Abernathy
Professor of Materials Science and
Engineering

I certify that I have read this study and that in my opinion it conforms to acceptable standards of scholarly presentation and is fully adequate, in scope and quality, as a dissertation for the degree of Doctor of Philosophy.



Stephen J. Pearton
Distinguished Professor of Materials
Science and Engineering

I certify that I have read this study and that in my opinion it conforms to acceptable standards of scholarly presentation and is fully adequate, in scope and quality, as a dissertation for the degree of Doctor of Philosophy.



Susan B. Sinnott
Associate Professor of Materials Science
and Engineering

I certify that I have read this study and that in my opinion it conforms to acceptable standards of scholarly presentation and is fully adequate, in scope and quality, as a dissertation for the degree of Doctor of Philosophy.



Toshikazu Nishida
Associate Professor of Electrical and
Computer Engineering

This dissertation was submitted to the Graduate Faculty of the College of Engineering and to the Graduate School and was accepted as partial fulfillment of the requirements for the degree of Doctor of Philosophy.

May 2005

A handwritten signature in dark ink, appearing to read "Pramod Khargonekar", is written over a horizontal line.

Pramod Khargonekar
Dean, College of Engineering

Kenneth Gerhardt
Interim Dean, Graduate School